Supplementary Information

Lattice Chemistry Damping Stabilization Enables Voltage Stability and Oxygen Redox Reversibility in Li-Rich Layered Oxides

Lingcai Zeng,[a] Yaqian Wang,[b] Tong Li,[a] Bao Qiu,*[b] Jiajie Pan,[a] Haoyan Liang,[b] Junhao Li,*[c] Xiaolei Sun[a], Jianrong Zeng,[d] Kaixiang Shi,[a] Zhaoping Liu,*[b] Quanbing Liu*[a]

[a] Guangzhou Key Laboratory of Clean Transportation Energy Chemistry, Guangdong Provincial Key Laboratory of Plant Resources Biorefinery, School of Chemical Engineering and Light Industry, Guangdong University of Technology, Guangzhou 510006, China

[b] Ningbo Institute of Materials Technology & Engineering (NIMTE), Chinese Academy of Sciences (CAS), Ningbo 315201, China

[c] School of Environmental and Chemical Engineering, Foshan University, Foshan 528225, China

[d] Shanghai Synchrotron Radiation Facility, Shanghai Advanced Research Institute, Chinese Academy of Sciences, Shanghai 201204, China

* E-mails: qiubao@nimte.ac.cn, lijunhao66@fosu.edu.cn, liuzp@nimte.ac.cn, liuqb@gdut.edu.cn

Experimental section

Materials synthesis

Synthesis of $Li_{1.154}Ni_{0.141}Co_{0.131}Mn_{0.533}O_2$ (LLO: pristine)

The Li-rich layered oxide $Li_{1.154}Ni_{0.141}Co_{0.131}Mn_{0.533}O_2$ (denoted as LLO) was synthesized via a conventional co-precipitation method. The carbonate precursor, $Ni_{1/6}Co_{1/6}Mn_{4/6}CO_3$ was prepared as previously reported.[1] Briefly, stoichiometric amounts of $MnSO_4·H_2O$ (1126.5 g), $NiSO_4·6H_2O$ (438.083 g), and $CoSO_4·7H_2O$ (468.4965 g) were dissolved in 5 L of deionized water to form a 2.0 $mol·L^{-1}$ mixed sulfate solution with a Ni:Co:Mn molar ratio of 1:1:4. This solution was pumped into a 50 L continuous stirred tank reactor (CSTR) at a controlled rate. Simultaneously, 0.2 $mol·L^{-1}$ ammonia solution (as complexing agent) and 2 $mol·L^{-1}$ Na_2CO_3 solution (as precipitant) were co-fed into the reactor. The pH was precisely maintained at 7.0–8.0 by adjusting the feeding rates, with the reactor temperature set at 60 °C and a stirring speed of 800 rpm. The co-precipitation was maintained for 40 h, followed by 12 h aging at 200 rpm. The resulting slurry was filtered and centrifugally washed multiple times with deionized water at 60 °C to remove residual Na_2CO_3. After drying at 120 °C, the precursor powder was obtained.

The LLO cathode was synthesized via solid-state lithiation. The as-prepared precursor was thoroughly mixed with Li_2CO_3 at a molar ratio of 1:1.4, followed by a two-step heat treatment: pre-calcination at 500 °C for 5 h, and final calcination at 850 °C for 12 h in air. After furnace cooling to room temperature, the LLO powder was collected.

Synthesis of $Li_{1.148}Ni_{0.140}Co_{0.131}Mn_{0.543}Mg_{0.0046}O_2$ (Mg-gradient).

The Mg-gradient modified Li-rich cathode (denoted as LLOM) was synthesized using the same procedure as for LLO, except for the addition of a trace amount of Mg. Specifically, 0.5 mol% $MgSO_4·H_2O$ was introduced by adjusting the sulfate solution composition to include 1121 g $MnSO_4·H_2O$, 435.73 g $NiSO_4·6H_2O$, 465.98 g $CoSO_4·7H_2O$, and 12.3235 g $MgSO_4·H_2O$, all dissolved in 5 L deionized water to maintain a total metal ion concentration of 2.0 $mol·L^{-1}$. The following co-precipitation and lithiation steps were identical to those used for LLO.

Synthesis of $Li_{1.081}Ni_{0.141}Co_{0.133}Mn_{0.551}O_{1.965}F_{0.035}$ (NH_4F-treated).

The surface fluorination of LLO was performed using ammonium fluoride (NH_4F). Specifically, 0.2283 g of NH_4F (0.05 mol) was dissolved in 100 mL of anhydrous ethanol. Then, 5 g of LLO powder was added, and the mixture was stirred at 80 °C until the solvent completely evaporated. The resulting powder was ground thoroughly and calcined at 400 °C for 4 h in a muffle furnace with a heating rate of 5 °C·min^{-1}. After furnace cooling, the fluorinated LLO product was obtained and denoted as LLOF.

Synthesis of $Li_{1.13}Ni_{0.140}Co_{0.131}Mn_{0.539}O_{1.966}F_{0.034}$ (Mg-gradient and NH_4F-treated).

The dual-gradient LLOMF material was prepared by applying the fluorination procedure described above to the Mg-modified LLOM material. To tune the fluorine content, three different amounts of NH_4F (0.1347 g, 0.3772 g, and 0.1820 g) were used to treat 5 g of LLOM. The resulting samples were labeled LLOM-0.03F, LLOM-0.08F, and LLOM-0.1F, respectively. The sample treated with 0.2283 g NH_4F (0.05 mol) was referred to as LLOMF.

Synthetic fluorine-free control (LLOM–NH_4HCO_3).

NH_4HCO_3 was prepared by replacing NH_4F with an equivalent molar amount of NH_4HCO_3 while keeping the post-treatment and annealing protocol identical to that of NH_4F treatment (see details above).

Materials characterizations.

Elemental concentrations and compositions of different electrodes before and after modification were analysed using an inductively coupled plasma optical emission spectrometer (ICP-OES, SPECTRO ARCOS II, SPECTRO) and a fluoride ion-selective electrode (F-ISE, Mercury-Sodium Electrode, PHS-3C). Synchrotron X-ray diffraction (SXRD) patterns were measured at the BL14B beamline of the Shanghai Synchrotron Radiation Facility (SSRF) using an X-ray wavelength of 0.6887 Å. Data were collected in the 2θ range of 10–40°. The microstructure of secondary particles before and after cycling was observed using field emission scanning electron microscopy (FESEM, Hitachi S-4800) and focused ion beam-scanning electron

microscopy (FIB-SEM, FEI Helios Nanolab 600i). HRTEM images of the pre- and post-cycling materials were characterised using a transmission electron microscope (S/TEM, ThermoFisher Talos-F200x). Electron paramagnetic resonance (EPR, E500) spectra were collected on a Bruker X-band A 200 computerised spectrometer at a microwave frequency of 9.8 GHz (X-band) and a microwave power of 2 mW. The magnetic field was modulated at a frequency of 100 kHz. The surface elemental composition of different cathode particles before and after cycling was observed using an X-ray photoelectron spectrometer (XPS, Kratos, Axis ultra DLD) at an electron energy of 1.487 keV. The samples were transferred from an argon-filled glove box to the XPS vacuum chamber via a sealed glass container. Depth profiling was performed using a 5 keV argon ion beam sputtering, with data collected every 15 nm, resulting in a total depth of 45 nm. The peak positions of surface elements were calibrated using the graphite peak at 284.8 eV in the C 1s spectrum. Elemental concentration depth profiles were characterised using TOF-SIMS (TOF.SIMS 5–100) at a pressure of 10^{-9} Torr. During the analysis, both pre- and post-cycling sample particles were bombarded with a 30 keV bismuth pulse beam, with a sampling area of 50×50 μm^2. The vibrational modes of chemical bonds on the surfaces of different cathode materials before and after cycling were studied using a confocal Raman spectrometer (Raman, Renishaw, Renishaw inVia Reflex) and a 532 nm laser. The distribution of elemental concentrations was further characterized by TEM (TF20) equipped with an energy spectrometer and electron energy loss spectroscopy (EELS). The specific surface area and mesopore analysis of different cathode samples were conducted using a fully automatic specific surface area and porosity analyser (BET, Micromeritics Instrument, HD88). The specific surface area and pore distribution of the materials were analysed using physical low-temperature nitrogen adsorption combined with the Brunauer-Emmet-Teller equation. Hard X-ray absorption spectroscopy (hXAS) experiments were carried out with transmission mode at beamline BL13SSW of the Shanghai Synchrotron Radiation Facility (SSRF) in Shanghai, China. The Athena software package[2] was used to process and fit the X-ray absorption near-edge structure (XANES) and extended X-ray absorption fine structure (EXAFS) data. Neutron powder diffraction (NPD) patterns

were obtained at the GPDD beamline of China Spallation Neutron Source (CSNS). The joint refinements using NPD and SXRD data were performed by the GSAS-II program based on the Rietveld method.[3]

Determination of XANES Edge Position via the Integral Method (Adapted from the Approach by H. Dau et al.) [4]

(1). Spectrum Normalization and Edge Interval Definition

Each absorption spectrum μ(E) was first subjected to pre-edge background subtraction and post-edge normalization, such that the pre-edge baseline approaches 0 and the post-edge plateau approaches 1. Two absorption thresholds, μ1 and μ2, were defined within the normalized edge rise region: following the original protocol, μ1 was set to 0.2 to avoid pre-edge interference, and μ2 to 1.00 to correspond to the fully developed edge step. An energy window [E1, E2] was then selected to satisfy μ(E1) < μ1 and μ(E2) > μ2, ensuring full coverage of the edge rise.

(2). Truncated Absorption Function for Non-Monotonicity Correction

To address potential non-monotonic fluctuations in experimental μ(E) caused by noise, a truncated absorption function μE was defined:

μE= μ1 when μ(E)< μ1

μE= μ2 when μ(E)> μ2

μE= μ(E) otherwise

This treatment ensures uniquely defined and numerically stable integration bounds.

(3). Integral Calculation of Edge Position

The edge position Eedge was calculated as:

$$E_{edge} = E_1 + \frac{1}{\mu 2 - \mu 1}\int_{E1}^{E2} (\mu 2 - \mu E)\,dE$$

In practice, the integral was evaluated using the trapezoidal rule over the measured energy grid. When [E1, E2] is chosen to span the full rise from below μ1 to above μ2, Eedge is insensitive to the specific values of E1 and E2, and primarily determined by the fixed parameters μ1 and μ2.

(4). Valence Calibration Using Reference Compounds To convert E_{edge} to an average oxidation state, reference compounds with known formal valences (e.g., Li_2MnO_3, Mn_2O_3) were measured under identical conditions. A linear calibration relationship was established:

$$E_{edge} = a + b * n_{ox}$$

where nox is the formal oxidation number, and a, b are obtained via linear regression. The average oxidation state of electrodes at different states of charge was then determined by substituting the measured E_{edge} into the calibrated equation. The same μ1, μ2, normalization protocol, and fitting procedure were applied consistently to all spectra to ensure reliable comparison.

Electrochemical measurements

Mix the cathode material with polyvinylidene fluoride (PVDF) and Super-P (SP) in N-methyl-2-pyrrolidone (NMP) at a mass ratio of 8:1:1. The slurry is coated onto aluminium foil at a thickness of 400 μm and dried for 4 hours in an 80 °C forced-air drying oven and for 12 hours in a 120 °C vacuum drying oven. The active material loading of the cathode electrode is approximately 7 mg cm^{-2}. The CR2032 button battery was assembled in an argon-filled glove box, with lithium metal as the anode and Celgard 2502 as the separator. 1 M $LiPF_6$ is dissolved in ethylene carbonate and diethyl methyl carbonate in a volume ratio of 3:7. The battery was subjected to constant-current charge-discharge cycling within a voltage range of 2.0–4.6 V (relative to Li^+/Li^0) using the WHW-200L-160CH-B battery testing system at room temperature. The battery was first activated three times at a current density of 0.1 C (1 C = 250 mA g^{-1}). In situ/ex situ electrochemical impedance spectroscopy (EIS) tests were conducted using a dual potentiostat (CHI760F) from Shanghai Chenhua Instrument Co., Ltd. within a frequency range of 100 kHz to 0.01 Hz. The cyclic voltammogram (CV) curves were tested using an Autolab electrochemical workstation. Li^+ diffusion coefficients were determined using CV curves acquired at varying scan rates:

$$I_p = (2.69 * 10^5) n^{\frac{3}{2}} C_{Li} A v^{\frac{1}{2}} D_{Li}^{\frac{1}{2}}$$

Specifically, n (number of transferred electrons), C_{Li} (molar concentration of Li^+ per unit volume), and A (electrode surface area) are constants throughout the experiment. The peak current (I_p) and scan rate (v) were extracted from CV profiles measured at

selected scan rates. Based on the Randles–Sevcik equation,[5] a linear fit was conducted with $v^{1/2}$ as the independent variable and I_p as the dependent variable, where the slope of the fitted line reflects the magnitude of the Li^+ diffusion coefficient. The constant current intermittent titration technique (GITT) was performed using a cycle of 10 minutes of charging and 1 hour of relaxation. The Li^+ diffusion coefficient was calculated using the following simplified formula:

$$D_{Li^+} = \frac{4}{\pi\tau}\left(\frac{mV_M}{MS}\right)^2\left(\frac{\Delta E_S}{\Delta E_\tau}\right)^2$$

The pouch cells are assembled using graphite (64 mm × 74 mm) as the negative electrode and LLOMF (62 mm × 72 mm) as the positive electrode. The anode electrode consists of graphite (93.5%), KS-6 (1.0%), SP (1.0%), SWCNTs (0.5%), styrene-butadiene rubber (SBR, 2.3%), and water-soluble binder (CMC, 1.7%), with the slurry coated onto copper foil. The cathode consists of active material (92%), PVDF (2.0%), carbon nanotubes (1.0%), KS-6 (2.16%), SP (2.0%), and single-walled carbon nanotubes (SWCNTs, 0.84%), with the slurry coated onto aluminium foil. The active material loading of the cathode is 10 mg cm^{-2}, and that of the anode is 7.8 mg cm^{-2}, with an N/P ratio set to 1.08. Additionally, the Compaction density of the LLOMF cathode is 2.3 g cm^{-3}, and the packing density of the graphite anode is 1.6 g cm^{-3}. A 1.5 Ah graphite||LLOMF pouch battery was assembled in a drying chamber (relative humidity 30%, 25 °C). The electrolyte was injected at a rate of 3 g Ah^{-1} in an argon glove box. The pouch battery was subjected to constant current charge-discharge cycling tests using the NEWARE-CT4008 battery testing system within a voltage window of 2.0–4.55 V (*vs.* Li^+/Li^0).

DFT Calculation

The first-principles calculations were performed within the density functional theory framework by using the projector augmented wave (PAW) method, as implemented in the Vienna ab initio simulation package (VASP),[6, 7] which is based on density functional theory (DFT). We adopted the spin-polarized generalized gradient approximation (GGA)+U method with Perdew-Burke Ernzerhof (PBE) exchange-correlation function for formation energy, and Meta-GGA for density of state, where the U values were 6.2 for Mn in the $Li_{32}Mn_{16}O_{48}$ system.[8, 9] The energy and force convergence values were chosen as 10^{-4} eV and 0.03 eV $Å^{-1}$, respectively. The Kohn-Sham orbitals were expanded in plane waves with a kinetic energy cut-off of 520 eV. The Brillouin zone

integration and k-point sampling were performed with a Monk Horst-Pack scheme of a 3 × 3 × 3 grid with Γ symmetry for all calculations.[10] The formation energy of Mg/F doped and oxygen vacancy formation in LLO was calculated based on the total energy of LLO by the reported approach.[11, 12]

The formation energies (E_{dop}) of each doping site and doping element were calculated. Taking the Li site occupied by Mg as an example, E_{dop} is described by the following equations:

$$E_{dop} = E(Li_{31}Mn_{16}O_{48}) - E(Li_{32}Mn_{16}O_{48}) - E(Mg) + E(Li)$$

Where $E(Li_{32}Mn_{16}O_{48})$ and $E(Li_{31}Mn_{16}O_{48})$ are the total energy of the system before and after one Li site is occupied by Mg, respectively. E(Li) and E(Mg) are the energy of Li and Mg single atoms, respectively.

The oxygen vacancy formation energy (E_{ov}) was calculated by the following equations:

$$E_{ov} = E(Li_{32}Mn_{16}O_{47}) - E(Li_{32}Mn_{16}O_{48}) + 1/2\ E(O_2)$$

Where $E(Li_{32}Mn_{16}O_{47})$ and $E(Li_{32}Mn_{16}O_{48})$ are the total energy of the system with and without oxygen vacancy and $E(O_2)$ is the chemical potential of O_2.

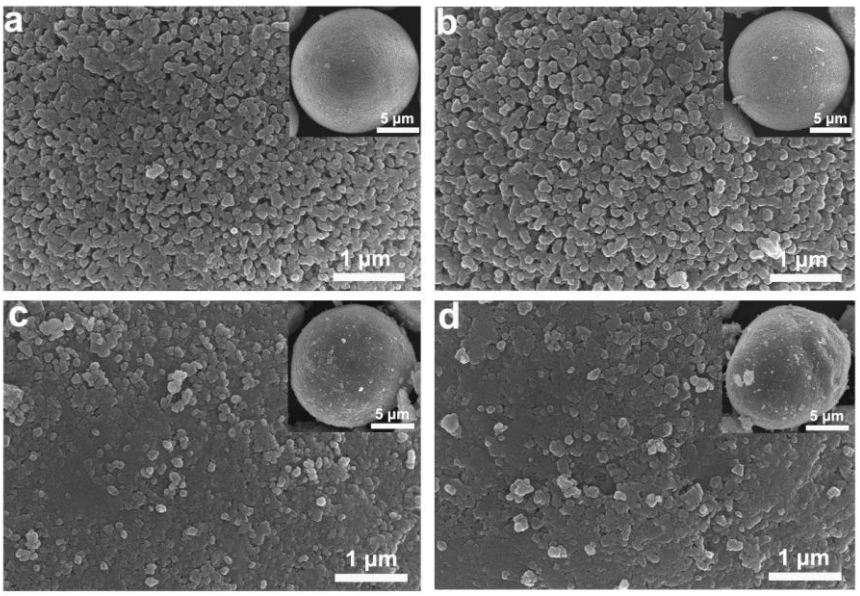

Fig. S1 SEM images of (a) LLO, (b) LLOM, LROF; and (c) LLOMF.

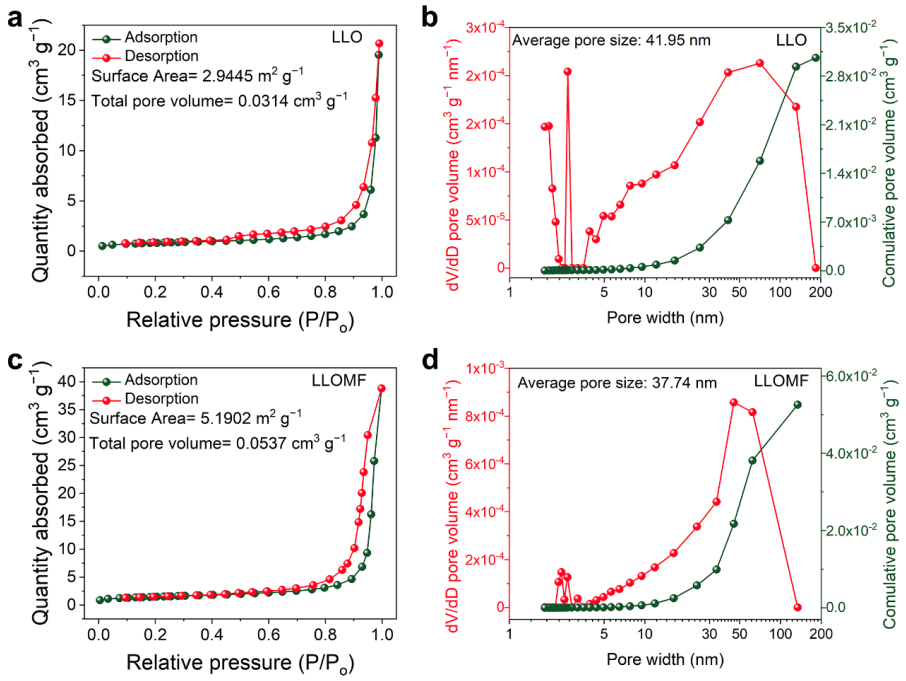

Fig. S2 Nitrogen adsorption-desorption isotherms of LLO (a) and LLOMF (c) samples, and pore size distribution of LLO (b) and LLOMF (d).

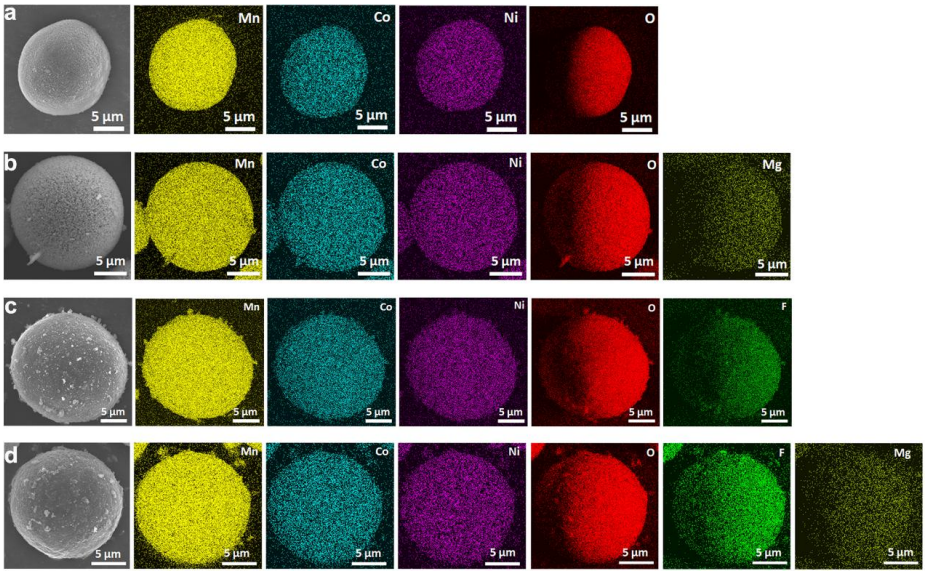

Fig. S3 EDS mapping of (a)LLO, (b) LLOM, (c) LROF, and (d) LLOMF.

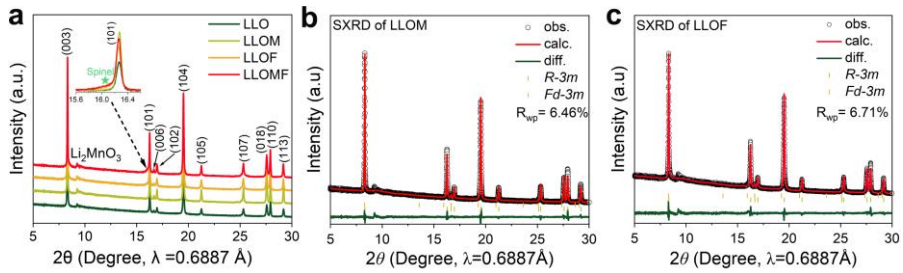

Fig. S4 (a) Synchrotron X-ray diffraction patterns of LLO, LLOM, LLOF, and LLOMF, and Rietveld refinement results of LLOM (b) and LLOF (c).

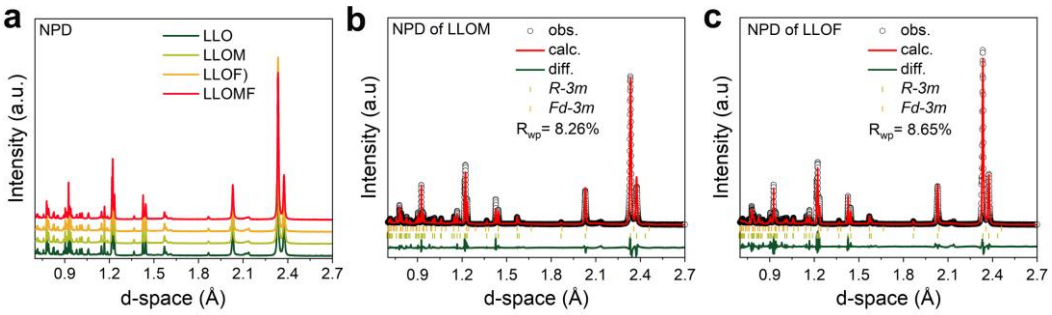

Fig. S5 (a) Neutron powder diffraction patterns of LLO, LLOM, LLOF, and LLOMF, and Rietveld refinement results of LLOM (b) and LLOF (c).

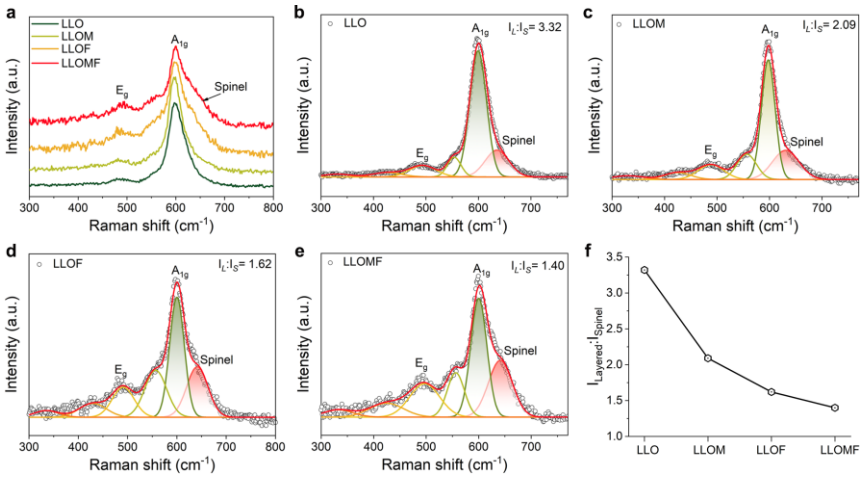

Fig. S6 (a-f) Raman spectra of LLO, LLOM, LLOF, and LLOMF samples and their fitting results.

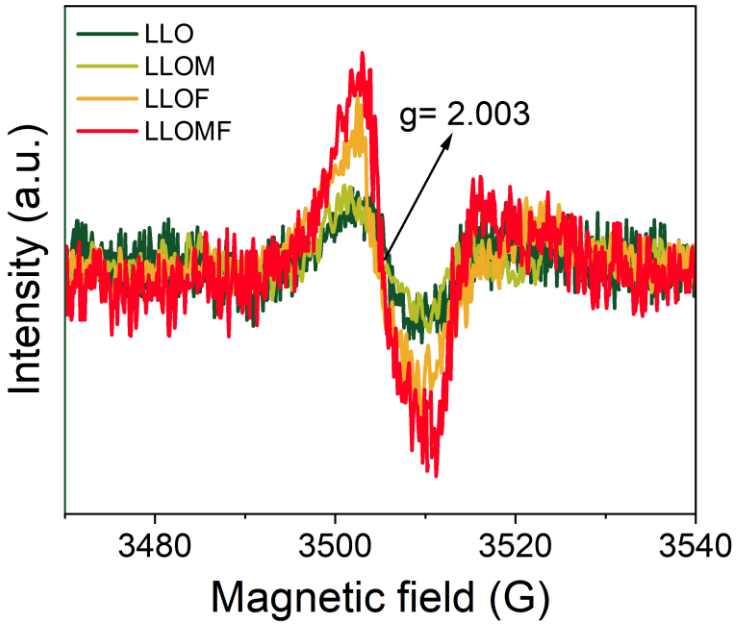

Fig. S7 Electron paramagnetic resonance (EPR) analysis was performed on LLO, LLOM, LLOF, and LLOMF samples.

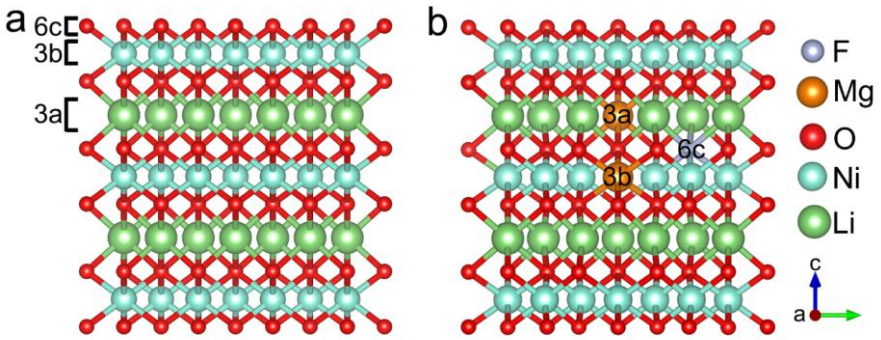

Fig. S8 (a) The crystal structure of $LiNiO_2$ and the atomic occupation positions of Li, Ni, and O atoms. (b) Schematic diagram of the binding sites of Mg and F atoms in typical $LiNiO_2$.(R-3m).

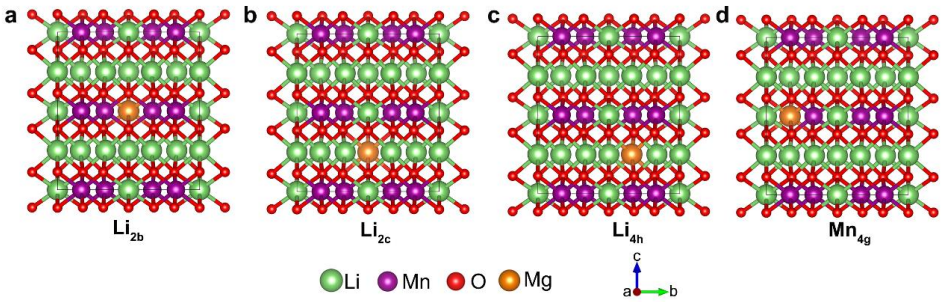

Fig. S9 Schematic diagrams showing the different occupation sites of the Mg atom in the Li_2MnO_3 (C2/m) lattice.

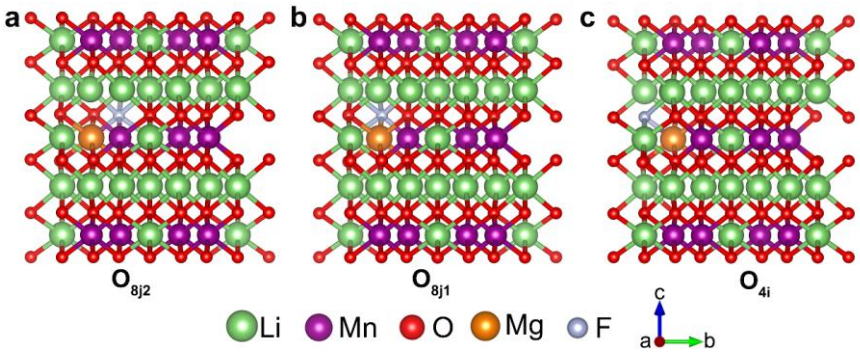

Fig. S10 Schematic diagrams showing the different occupation sites of the F atom in the Mg-Li_2MnO_3 lattice.

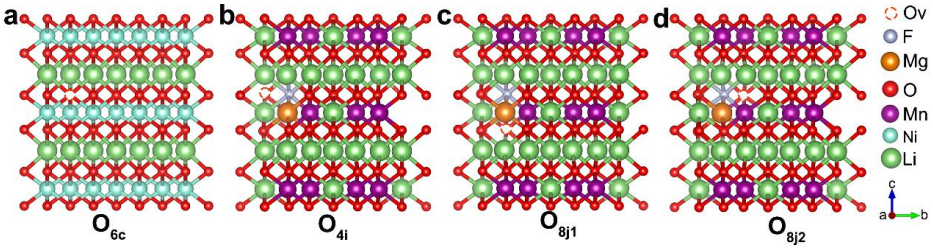

Fig. S11 The schematic diagram shows the different occupancy sites of oxygen vacancies in the Mg/F-doped Li_2MnO_3 (C2/m) and $LiNiO_2$ (R-3m) lattices.

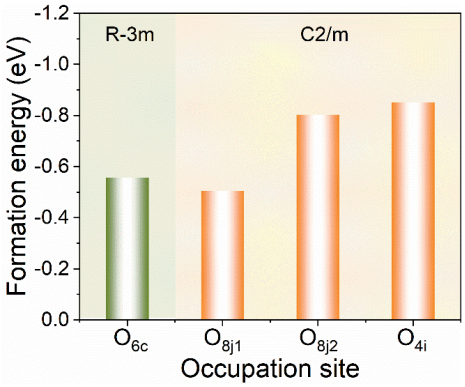

Fig. S12 Formation energies of different oxygen vacancy (Vo) sites in Mg/F-doped Li_2MnO_3 (C2/m) and $LiNiO_2$ (R-3/m).

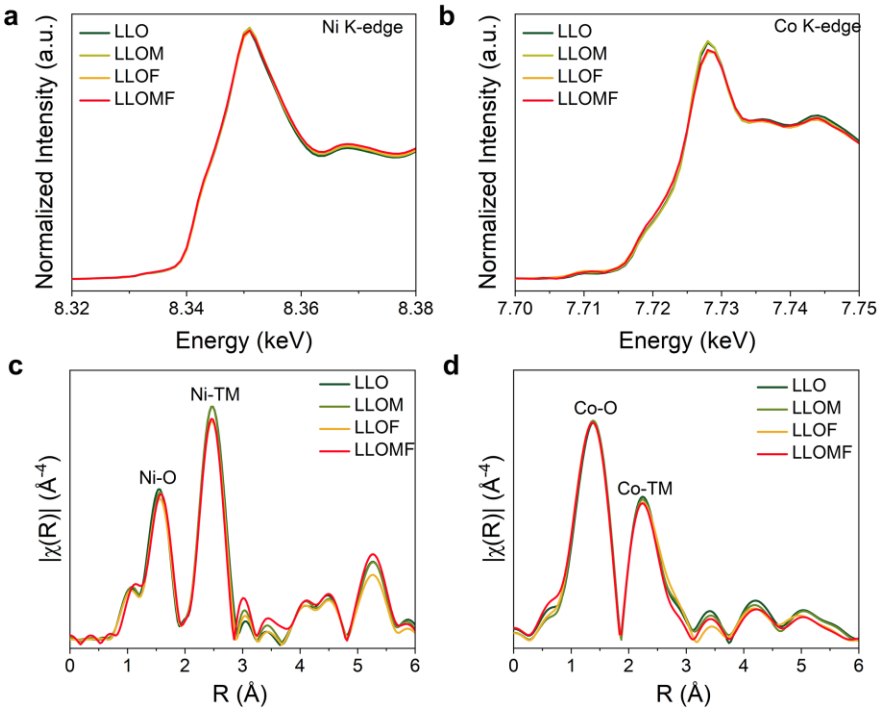

Fig. S13 (a, b) Normalized XANES spectra of Ni K-edge (a) and Co K-edge (b) for LLO, LLOM, LLOF, and LLOMF samples. (c, d) Fourier transform spectra of Ni K-edge (c) and Co K-edge (d) for LLO, LLOM, LLOF, and LLOMF samples from EXAFS.

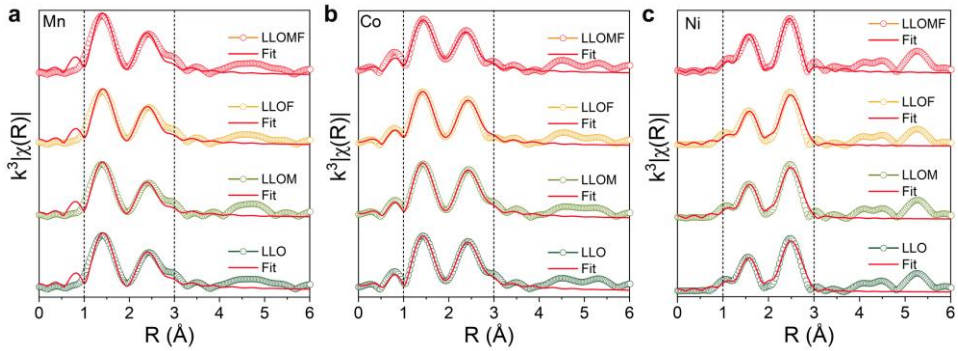

Fig. S14 a) Mn EXAFS fitting patterns of LLO, LLOM, LLOF, and LLOMF samples. b) Co EXAFS fitting patterns of LLO, LLOM, LLOF, and LLOMF samples. c) Ni EXAFS fitting patterns of LLO, LLOM, LLOF, and LLOMF samples. All spectra were fitted only to the first two coordination shells.

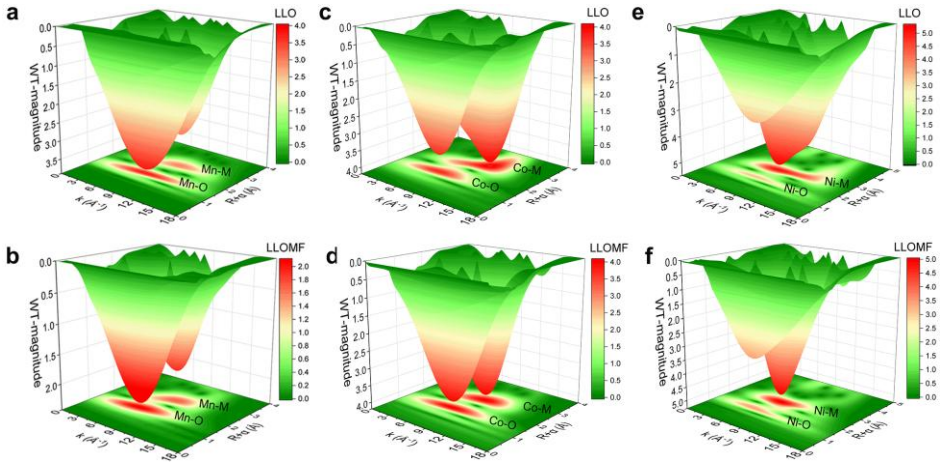

Fig. S15 (a, b) 3D WT for the k^3-weighted EXAFS spectra of the Mn K-edge for LLO (a) and LLOMF (b). (c, d) 3D WT for the k^3-weighted EXAFS spectra of the Co K-edge for LLO (c) and LLOMF (d). (e, f) 3D WT for the k^3-weighted EXAFS spectra of the Ni K-edge for LLO (e) and LLOMF (f).

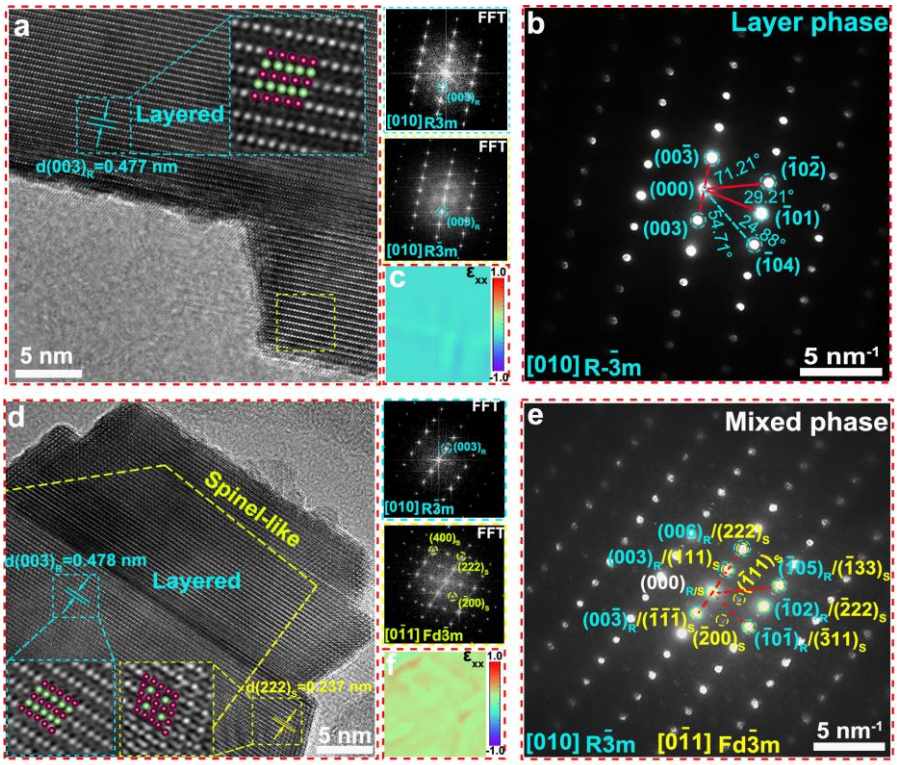

Fig. S16 (a, d) HRTEM image of LLOM (a) and LLOF (d). (b, e) SAED pattern of LLOM (b) and LLOF (e). (c, f) GPA patterns of LLOM (c) and LLOF (f).

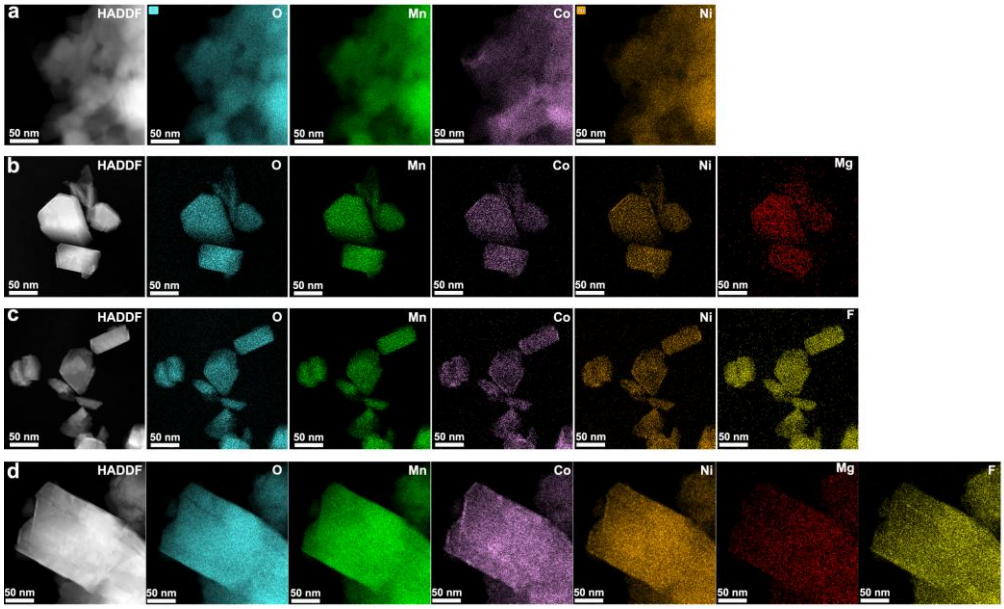

Fig. S17 HAADF-STEM and EDS mappings of Ni, Mn, Co, O, Mg, and F elements for LLO (a), LLOM (b), LLOF (c), and LLOMF (d) samples.

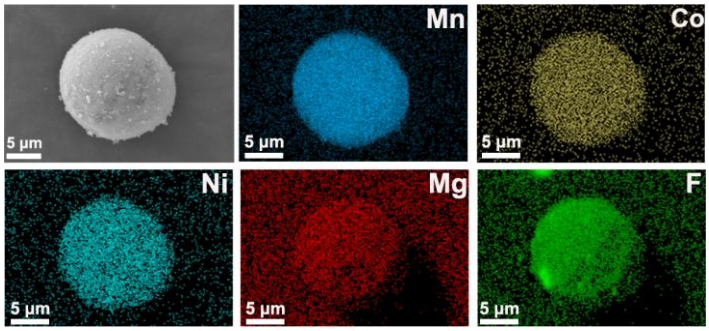

Fig. S18 EDS elemental distribution mapping of the surface of LLOMF secondary particles before cross-section treatment.

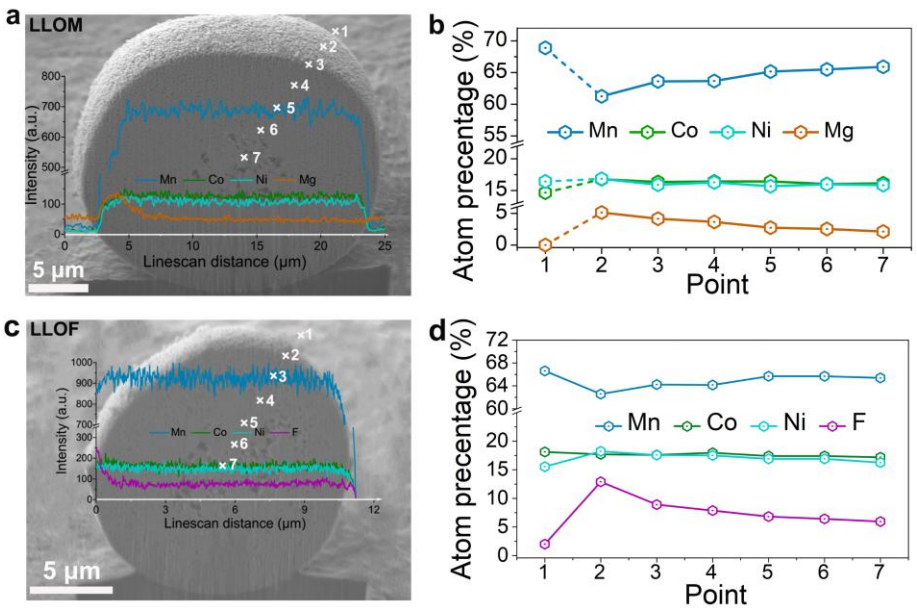

Fig. S19 (a, c) Cross-sectional Focused ion beam-scanning electron microscope (FIB-SEM) image and EDX line scan analysis across the LLOM (a) and LLOF (c) particle. (b, d) EDX point scanning analysis at the corresponding cross sections of LLOM (b) and LLOF (d).

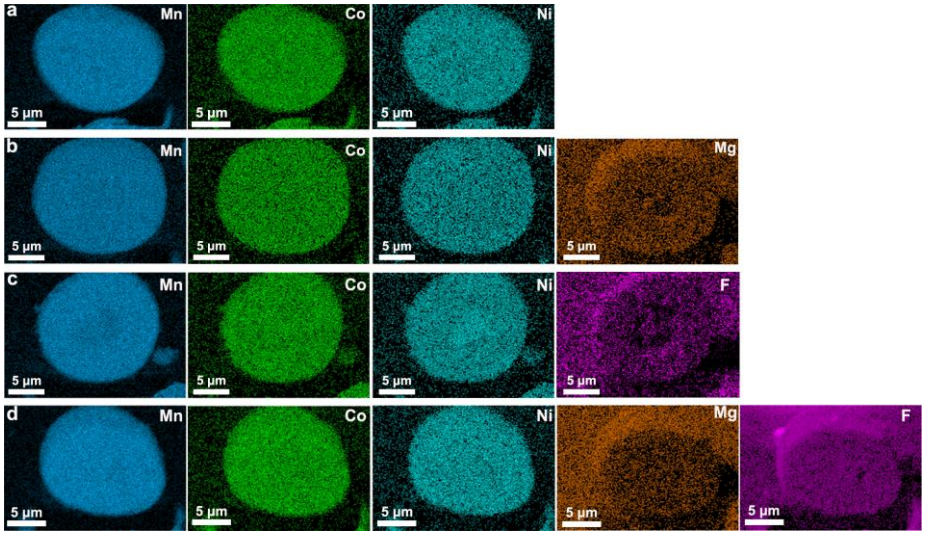

Fig. S20 SEM images show cross-sections of LLO (a), LLOM (b), LLOF (c), and LLOMF (d) samples and their corresponding EDS element distribution maps.

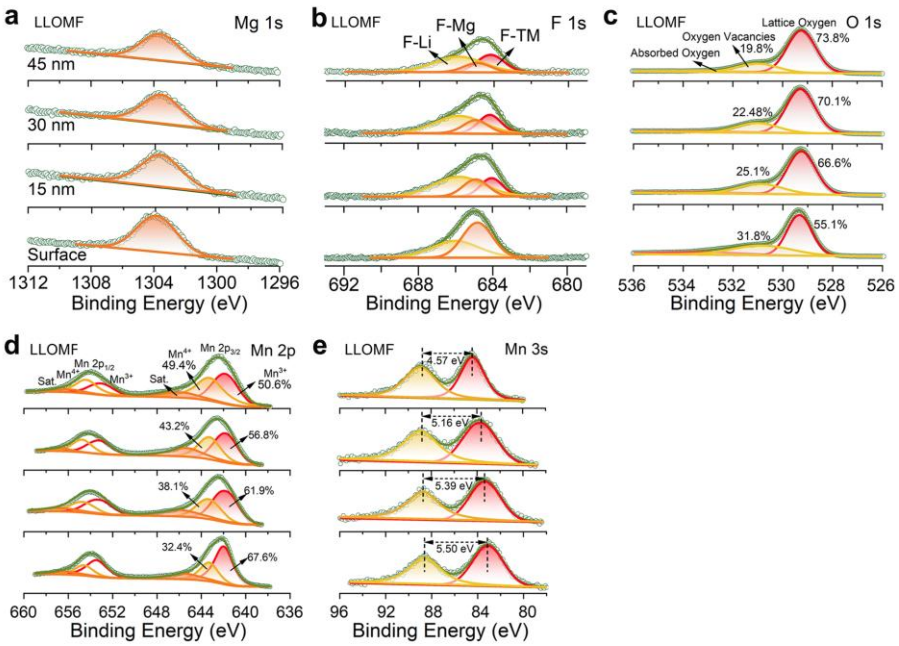

Fig. S21 (a~e) XPS spectra of Mg 1s (a), F 1s (b), O 1s (c), Mn 2p (d), and Mn 3s (e) for LLOMF samples with different etching levels.

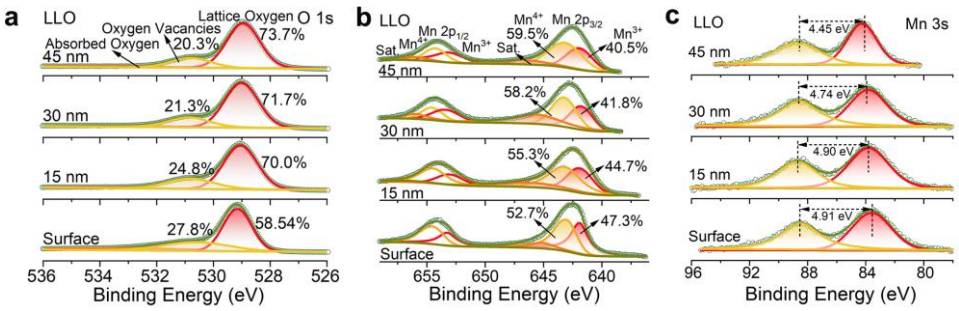

Fig. S22 (a~ c) XPS spectra of O 1s (a), Mn 2p (b), and Mn 3s (c) for LLO samples with different etching levels.

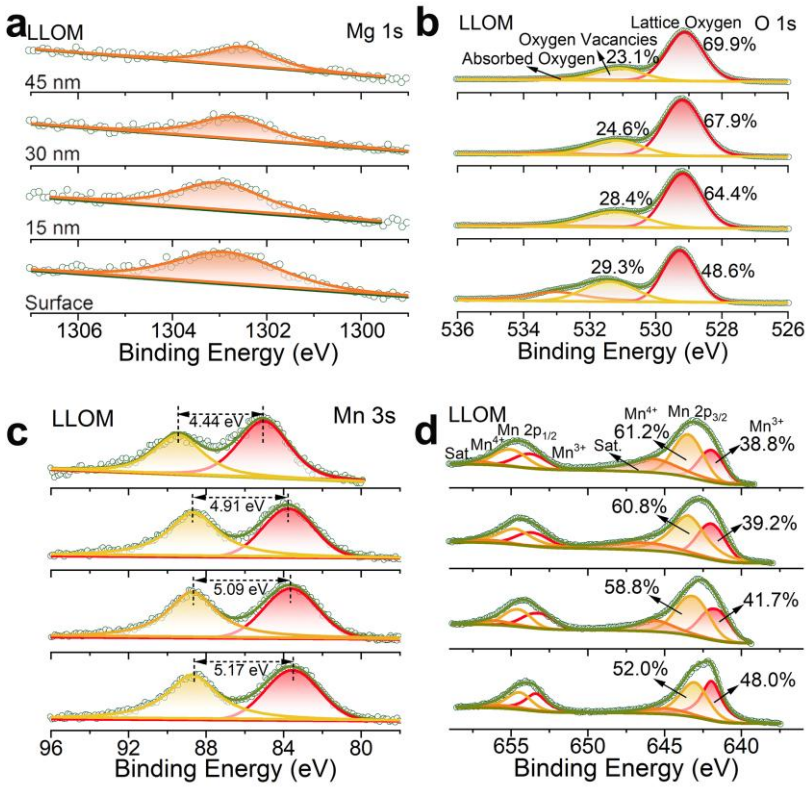

Fig. S23 (a~ d) XPS spectra of Mg 1s (a), O 1s (b), Mn 3s (c), and Mn 2p (d) for LLOM samples with different etching levels.

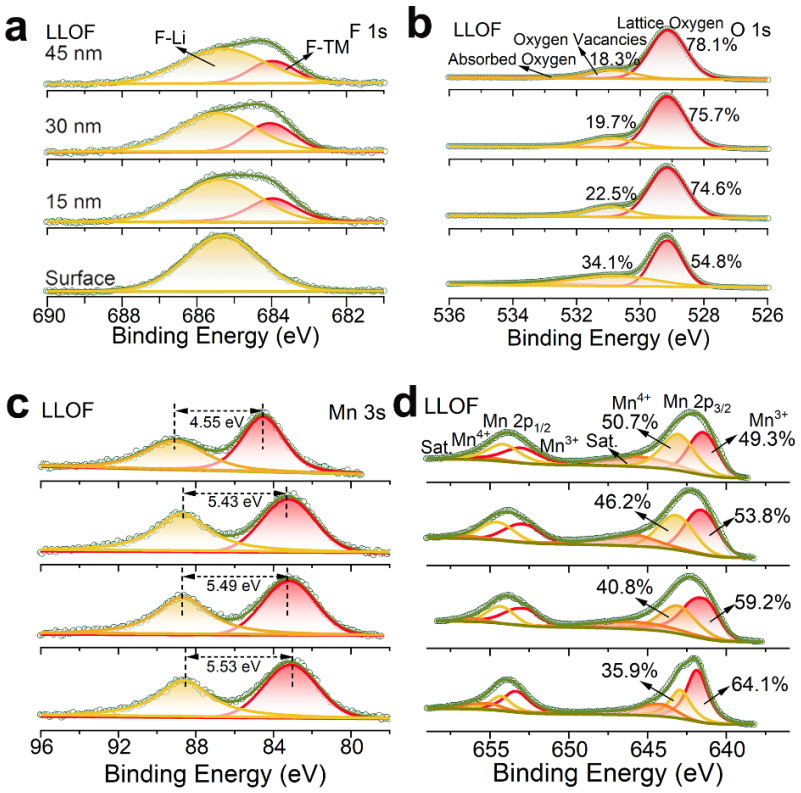

Fig. S24. (a~ d) XPS spectra of F 1s (a), O 1s (b), Mn 3s (c), and Mn 2p (d) for LLOF samples with different etching levels.

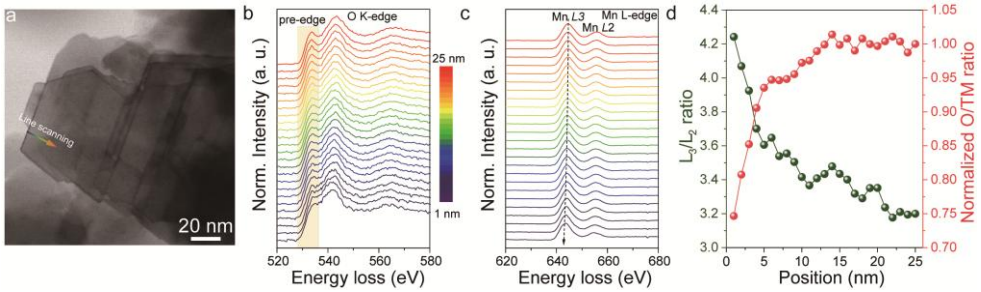

Fig. S25 Depth-resolved STEM-EELS characterization of LLOMF. (a) HAADF-STEM image with the EELS line-scan path indicated. (b) O K-edge spectra collected from the surface toward the bulk. (c) Mn L-edge spectra collected along the same line-scan. (d) Depth profiles of the Mn L_3/L_2 ratio and the normalized O/TM ratio as a function of distance from the surface.

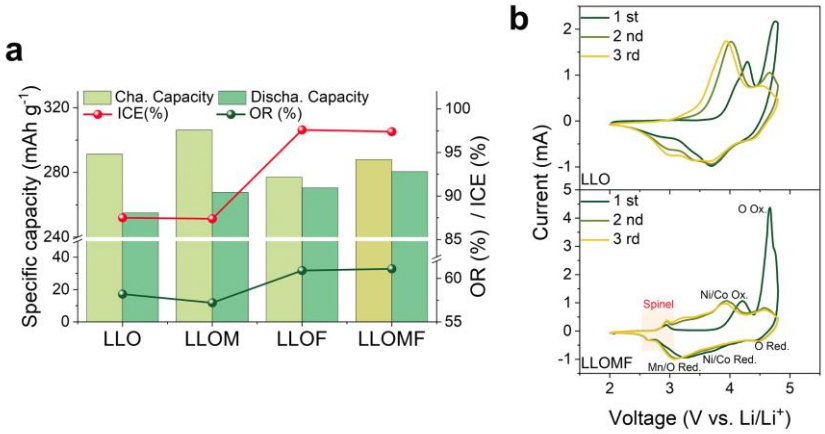

Fig. S26 (a) Charge capacity distribution and initial coulombic efficiency (ICE) of LLO, LLOM, LLOF and LLOMF. (b) CV plots of LLO (top) and LLOMF (bottom) at a scan rate of 0.2 mV s^{-1}.

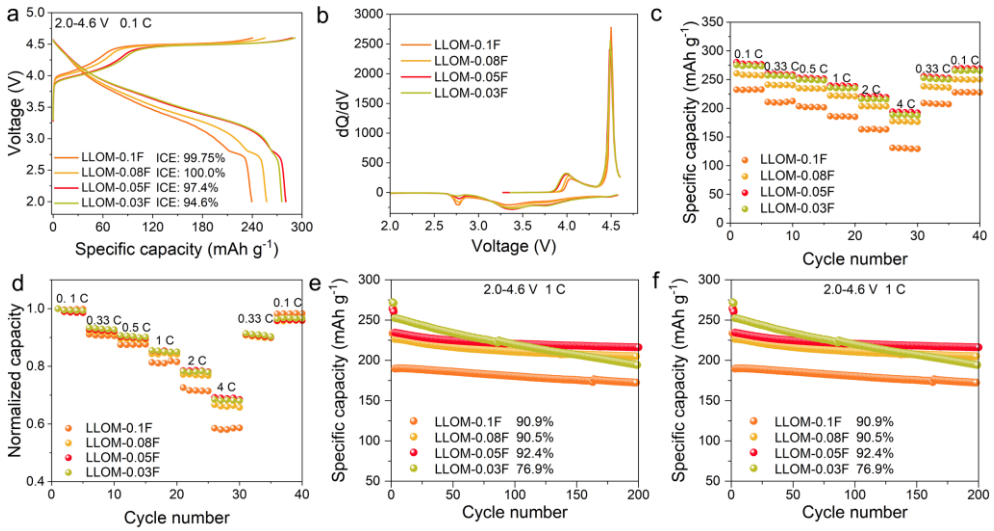

Fig. S27 Electrochemical performance of the Mg-fixed, F-tunable LLOM-xF series (x = 0.03, 0.05, 0.08, and 0.10). (a) Initial charge-discharge profiles at 0.1 C in the voltage window of 2.0–4.6 V. (b) Corresponding differential capacity (dQ/dV) curves. (c) Rate capability at stepwise current densities (0.1, 0.33, 0.5, 1, 2, and 4 C) with recovery to 0.33 C and 0.1 C. (d) Normalized rate performance derived from (c). (e) Cycling stability at 1 C (2.0–4.6 V). (f) Voltage stability at 1 C (2.0–4.6 V).

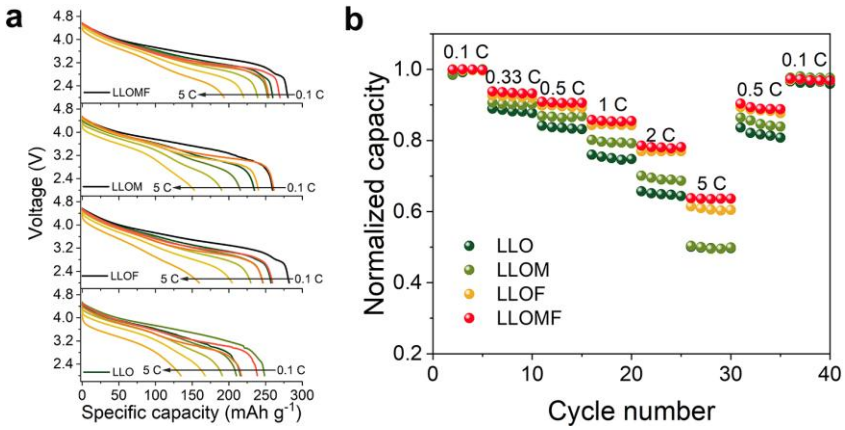

Fig. S28 (a) Capacity-voltage curves at different rates for LLO, LLOM, LLOF and LLOMF. (b) Normalised rate performance of LLO, LLOM, LLOF and LLOMF.

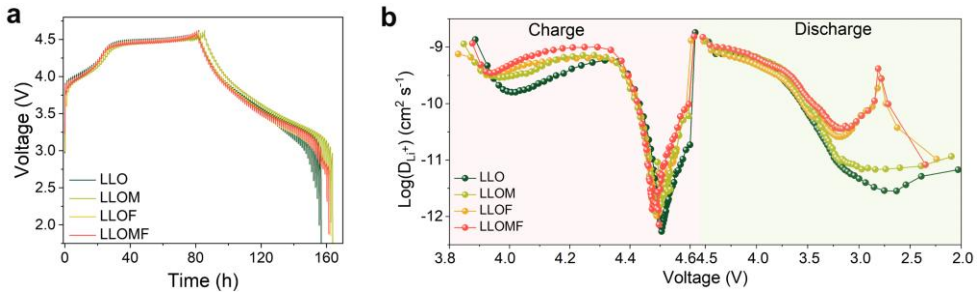

Fig. S29 (a, b) GITT curves (a) and corresponding D_{Li}^{+} coefficients (b) for the initial charge-discharge cycles of LLO, LLOM, LLOF, and LLOMF.

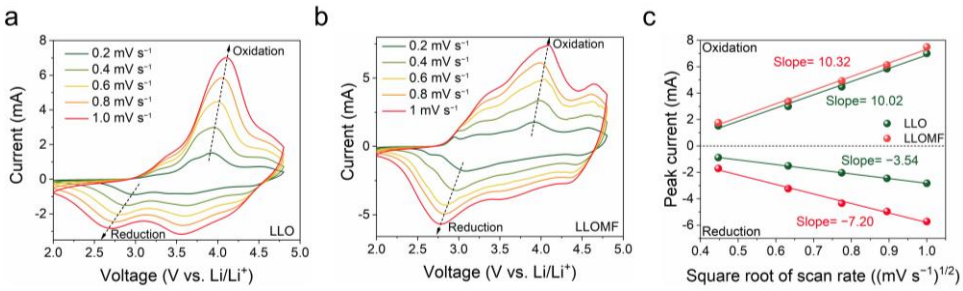

Fig. S30 CV curves of (a) LLO and (b) LLOMF samples at the selected scan rate. f) The current peaks (I_p) versus the square root of the selected scan rate ($\nu^{\frac{1}{2}}$) plots of the LLO and LLOMF; the fitting line of oxidation and the fitting line of reduction are shown as well.

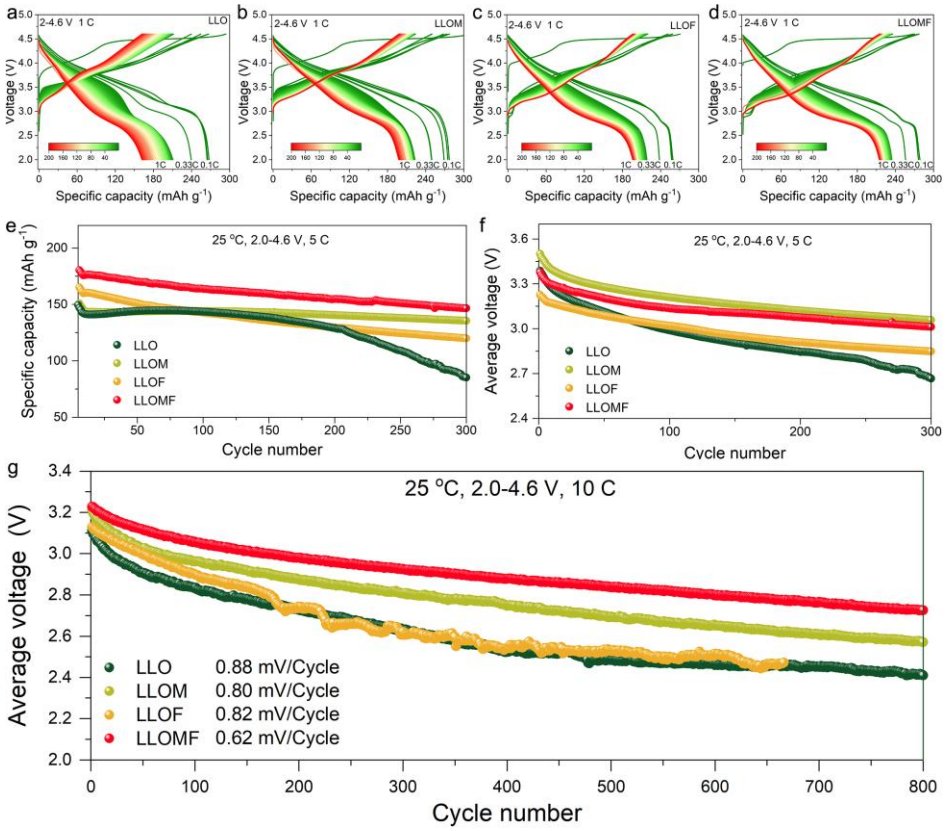

Fig. S31 (a~d) Capacity-voltage curves of LLO (a), LLOM (b), LLOF (c), and LLOMF (d) from the 1st cycle to the 300th cycle in the voltage range of 2.0−4.6 V. (e, f) Capacity fade (e) and Average discharge voltage decay (f) of LLO, LLOM, LLOF, and LLOMF during cycling at 5.0 C (1 C = 250 mA g^{-1}). (g) Average discharge voltage decay of LLO, LLOM, LLOF, and LLOMF during cycling at 10.0 C.

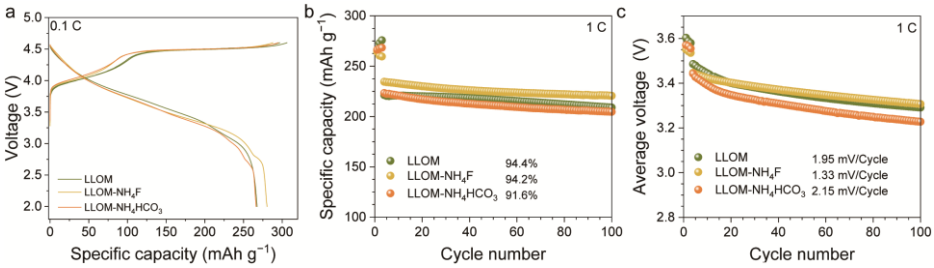

Fig. S32 Electrochemical performance of LLO, LLOM, LLOM-NH_4F, and LLOM-NH_4HCO_3 electrodes at 1 C: (a) Initial charge-discharge profiles; (b) Cycling stability; (c) Evolution of average voltage.

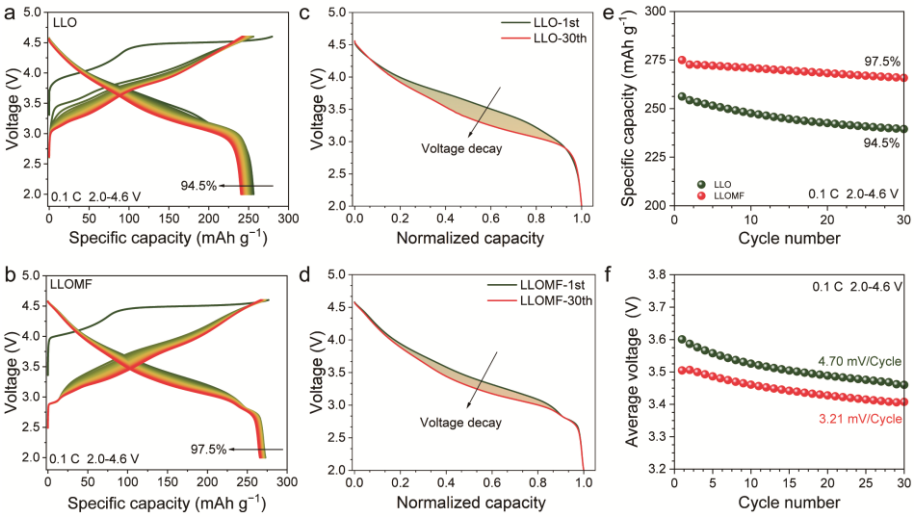

Fig. S33 Low-rate electrochemical behavior of LLO and LLOMF at 0.1 C within 2.0–4.6 V. (a) Galvanostatic charge-discharge voltage profiles of LLO at selected cycles. (b) Galvanostatic charge-discharge voltage profiles of LLOMF at selected cycles. (c) Normalized discharge voltage profiles of LLO at the 1st and 30th cycles, highlighting voltage evolution. (d) Normalized discharge voltage profiles of LLOMF at the 1st and 30th cycles. (e) Cycling performance of LLO and LLOMF at 0.1 C. (f) Evolution of average discharge voltage versus cycle number for LLO and LLOMF at 0.1 C.

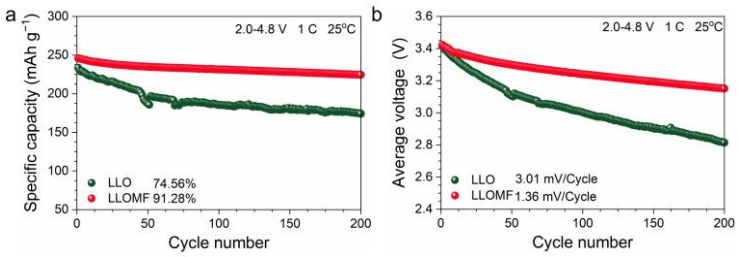

Fig. S34 Cycling performance of LLO and LLOMF cathodes at an elevated upper cut-off voltage. (a) Specific capacity retention versus cycle number measured in half-cells within 2.0–4.8 V at 1 C and 25 °C. (b) Evolution of average discharge voltage versus cycle number under the same conditions.

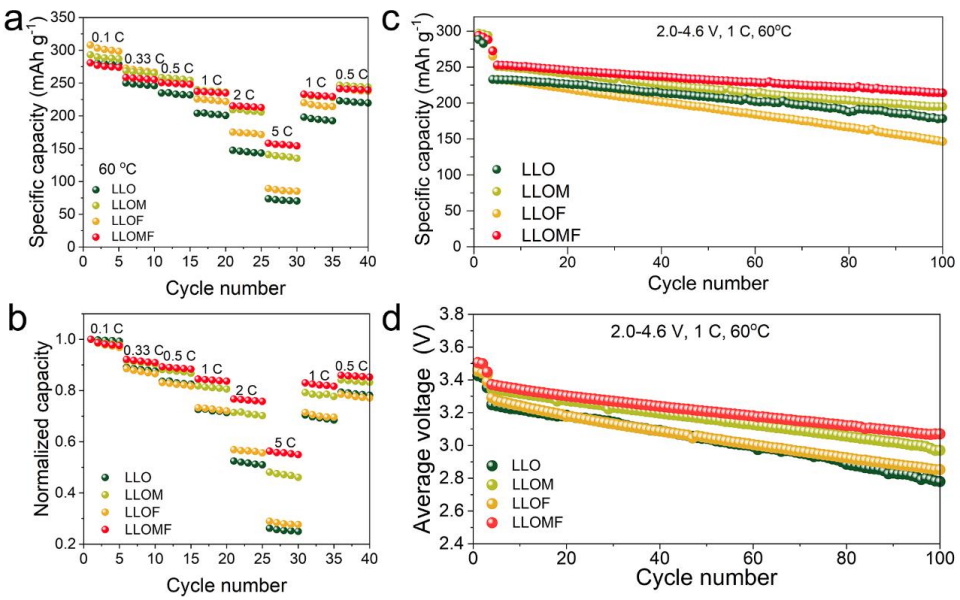

Fig. S35 (a, b) Rate performance (a) and normalised rate performance (b) of LLO, LLOM, LLOF, and LLOMF at 60ºC. (c, d) Capacity fade (c) and Average discharge voltage decay (d) of LLO, LLOM, LLOF, and LLOMF during cycling at 1.0 C and 60ºC.

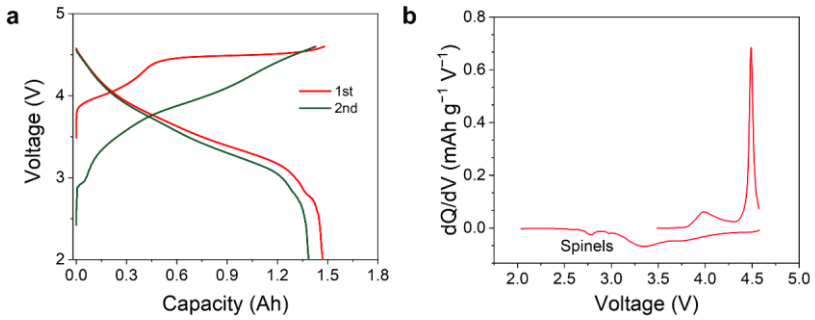

Fig. S36 (a) Charge–discharge profiles at the initial two cycles of the pouch-type graphite||LLOMF full cell within 2.0–4.6 V at 0.1 C. (b) The dQ/dV profiles obtained from the initial charge-discharge curve of graphite||LLOMF full cell.

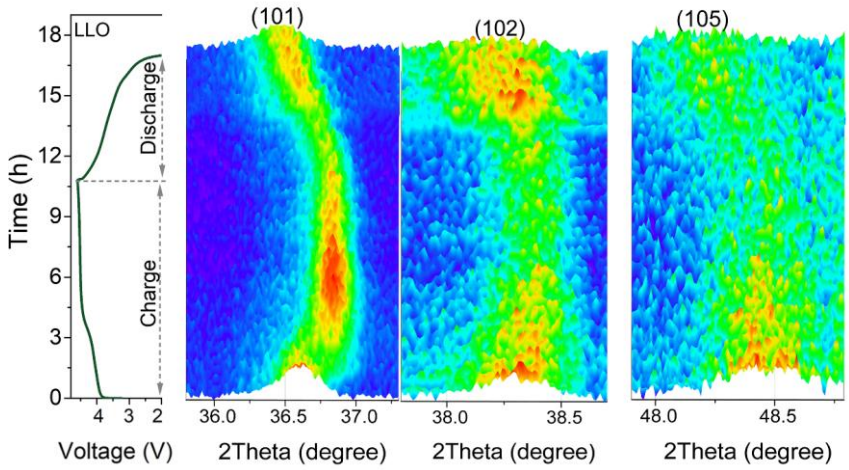

Fig. S37 Three-dimensional contour plots of (101), (102) and (105) peaks, which are derived from in situ XRD spectra of LLO electrodes, accompanied by time-potential curves at a charging rate of 0.1 C during the first cycle.

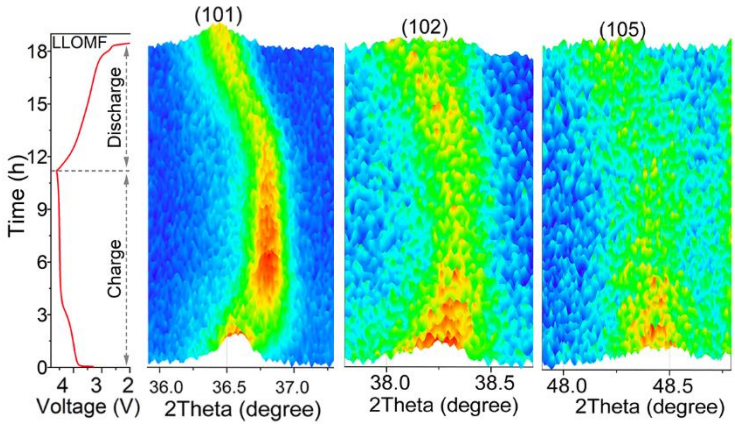

Fig. S38 Three-dimensional contour plots of (101), (102) and (105) peaks, which are derived from in situ XRD spectra of LLOMF electrodes, accompanied by time-potential curves at a charging rate of 0.1 C during the first cycle.

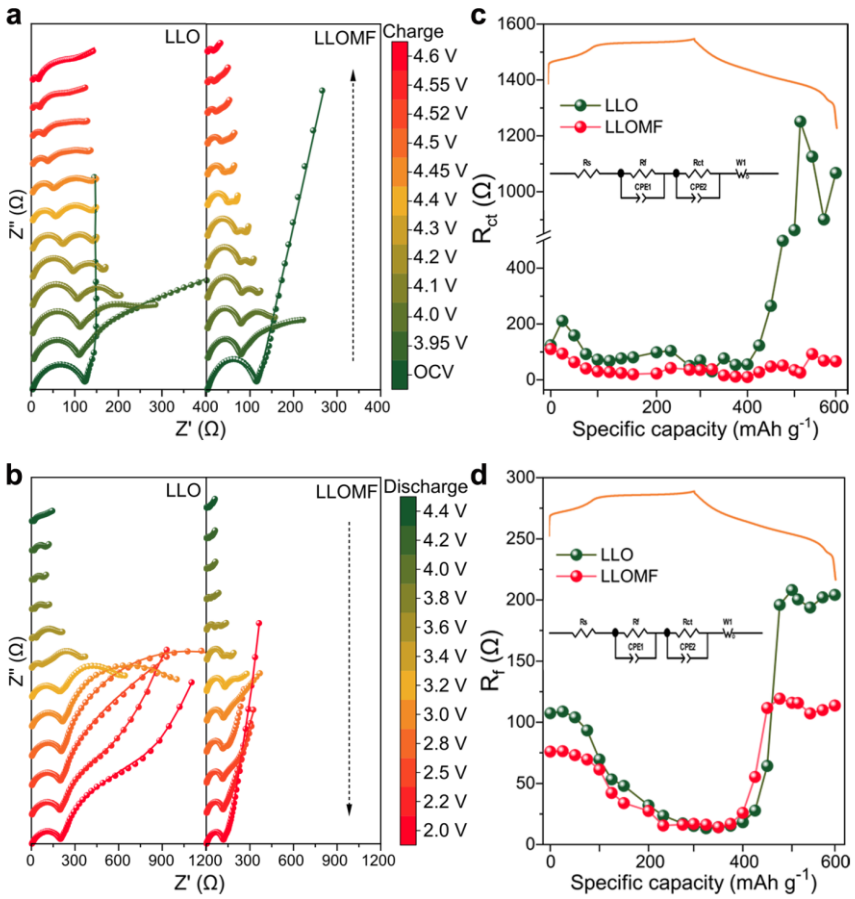

Fig. S39 In situ electrochemical impedance spectra of charging (a) and discharging (b) of LLO and LLOMF. c) The evolution of R_{ct} (c) and R_f (d) during the initial charge-discharge cycle. These data were obtained from the EIS Nyquist plot simulations in (a) and (b).

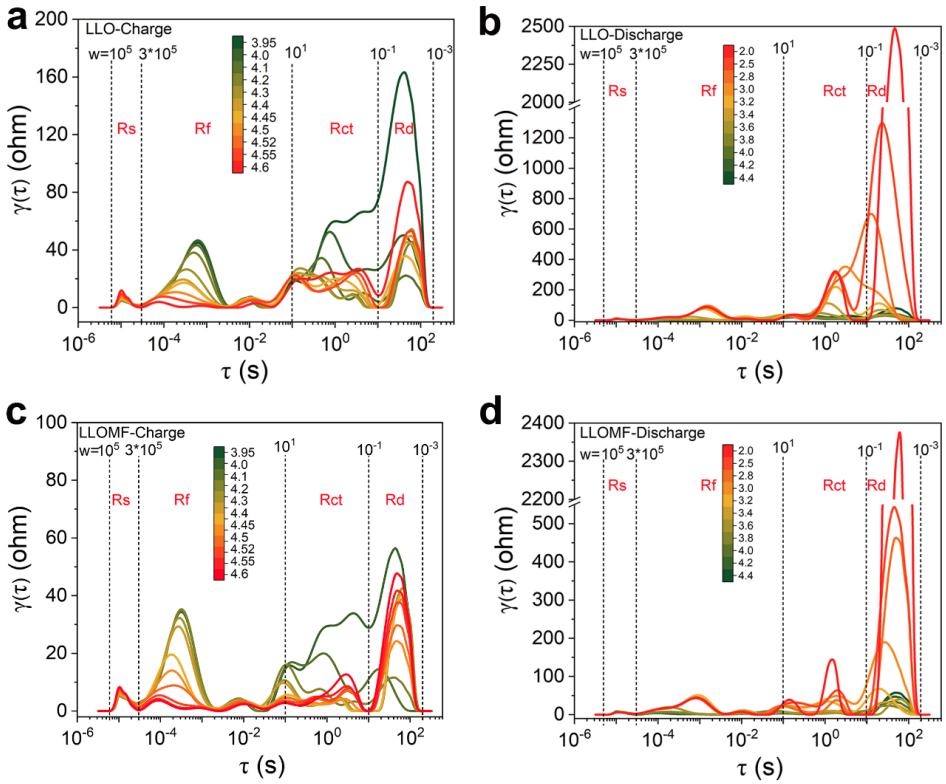

Fig. S40 (a~d) DRT curves calculated from in situ EIS measurement data obtained during corresponding charging/discharging processes based on LLO (a, b) and LLOMF (c, d).

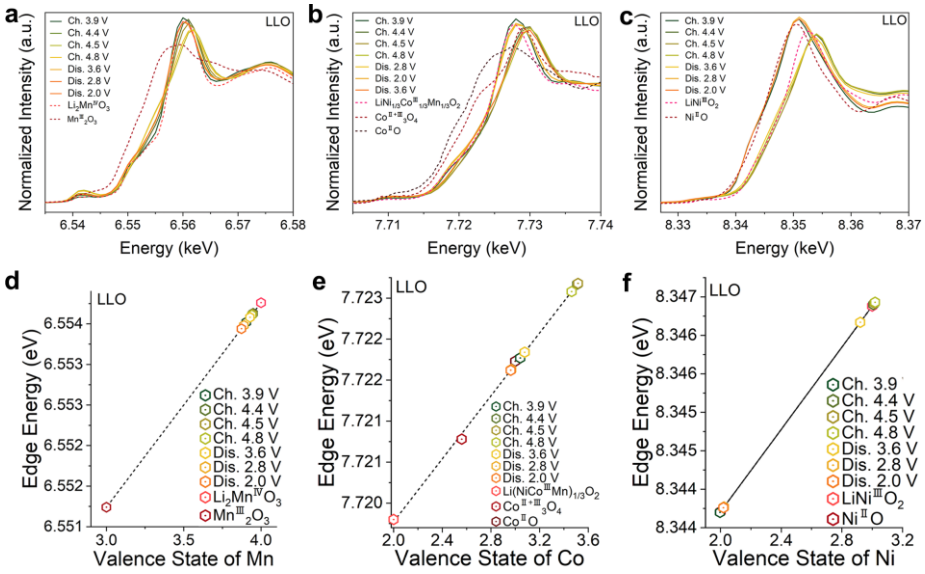

Fig. S41 Ex situ hard XAS of and LLO materials in the first cycle. (a~c) The normalized Mn K-edge (a), Co K-edge (b) and Ni K-edge (c) XANES spectra of LLO at different SOCs. (d~f)The valence state of Mn, Co and Ni in the Mn K-edge (d), Co K-edge (e) and Ni K-edge (f) X-ray absorption spectra of LLO samples in different SOCs was calculated using the integration method.

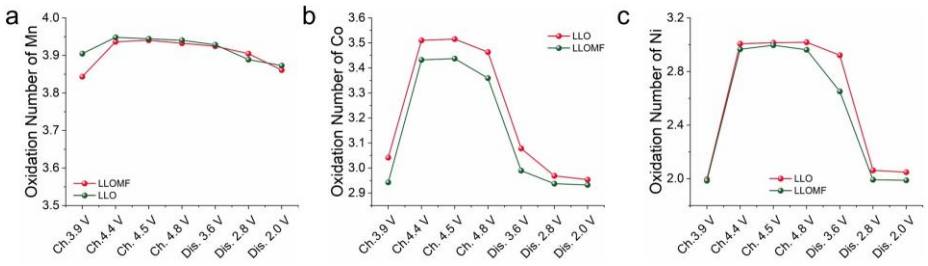

Fig. S42 Voltage-dependent evolution of the average Mn, Co and Ni oxidation states derived from XANES edge positions

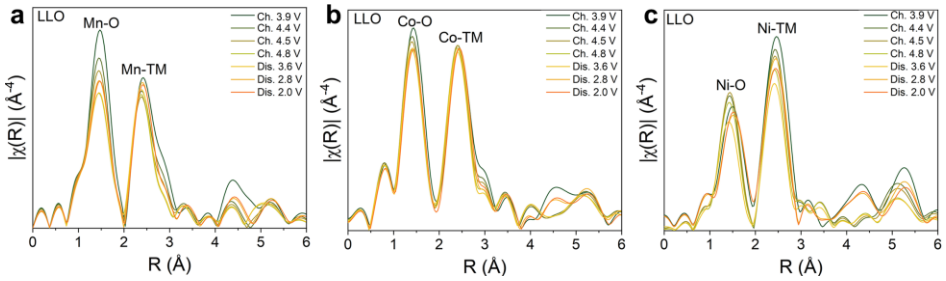

Fig. S43 (f) K-edge EXAFS spectra of Mn (a), Co (b) and Ni (c) for LLO samples at different SOCs during the initial charge–discharge.

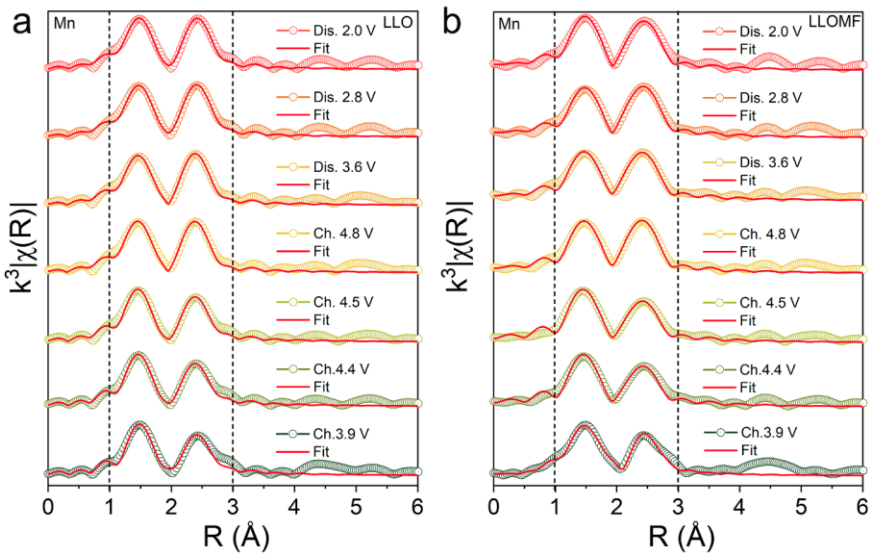

Fig. S44 Mn EXAFS fitting patterns of LLO (a) and LLOMF (b) at different SOCs during the first charge-discharge cycle. Only the first two coordination shells were fitted.

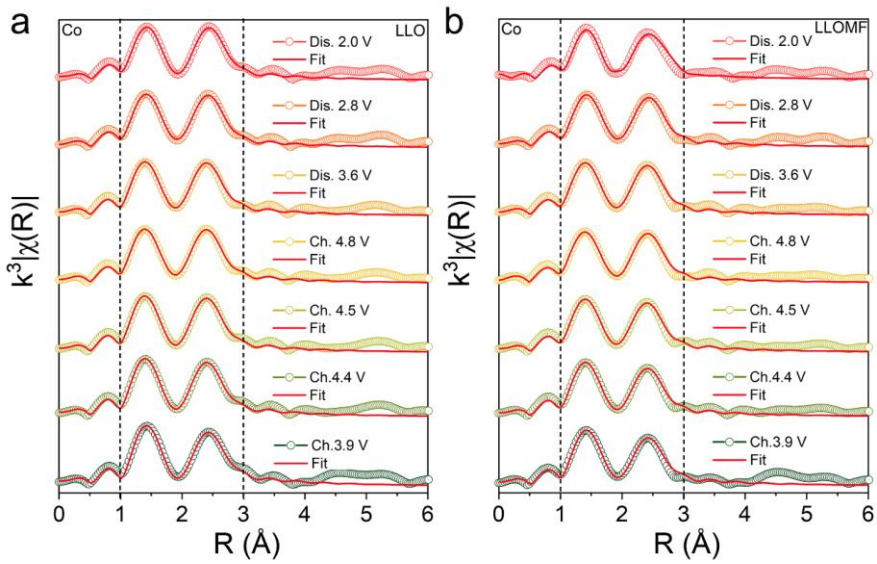

Fig. S45 Co EXAFS fitting patterns of LLO (a) and LLOMF (b) at different SOCs during the first charge-discharge cycle. Only the first two coordination shells were fitted.

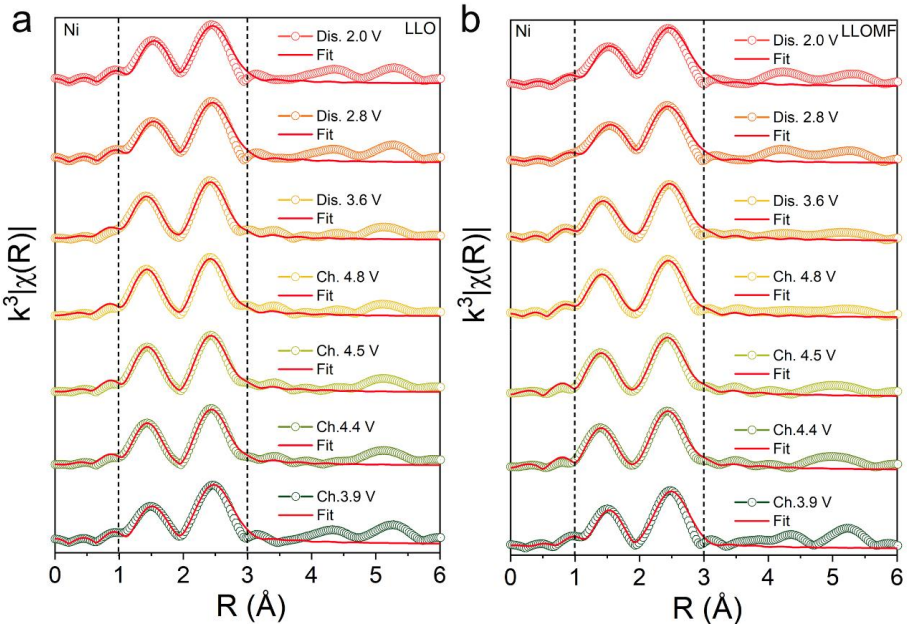

Fig. S46 Ni EXAFS fitting patterns of LLO (a) and LLOMF (b) at different SOCs during the first charge-discharge cycle. Only the first two coordination shells were fitted.

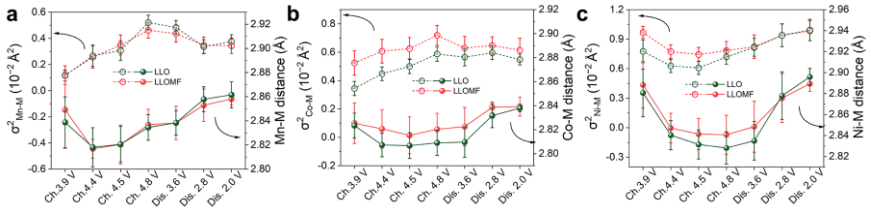

Fig. S47 (a) Evolution of the Mn–M coordination, including fitting the bond distance for the Mn–M bond and fitting the Debye–Waller factor for the Mn–O coordination environment, respectively, for LLO (green) and LLOMF (red). (b) Evolution of the Co–M coordination, including fitting the bond distance for the Co–M bond and fitting the Debye–Waller factor for the Co–M coordination environment, respectively, for LLO (green) and LLOMF (red). (c) Evolution of the Ni–M coordination, including fitting the bond distance for the Ni–O bond and fitting the Debye–Waller factor for the Ni–M coordination environment, respectively, for LLO (green) and LLOMF (red).

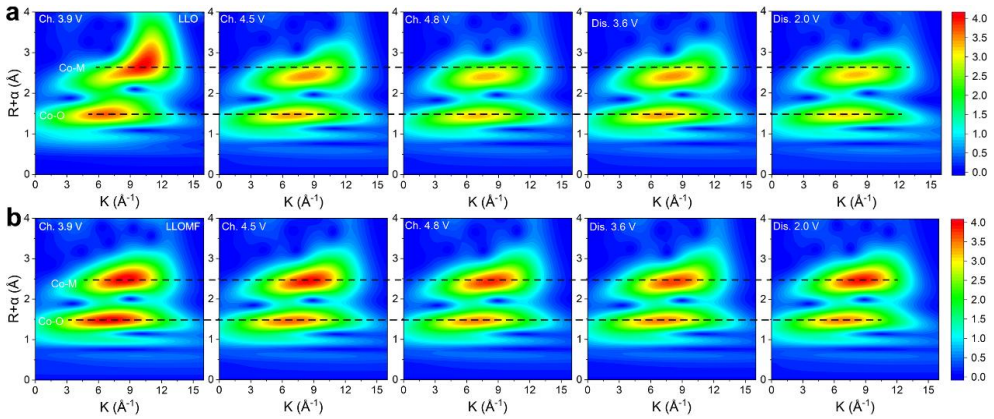

Fig. S48 Wavelet transform of Co K-edge EXAFS spectra of LLO (a) and LLOMF (b) at different SOCs during the first charge-discharge cycle.

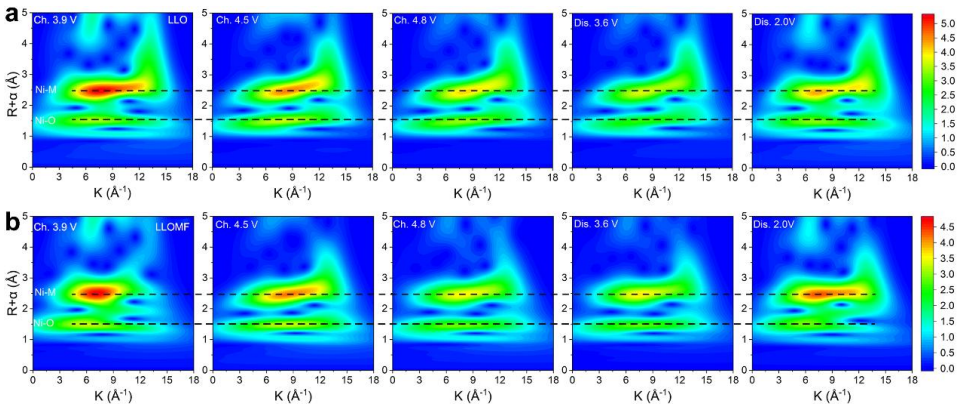

Fig. S49 Wavelet transform of Ni K-edge EXAFS spectra of LLO (a) and LLOMF (b) at different SOCs during the first charge-discharge cycle.

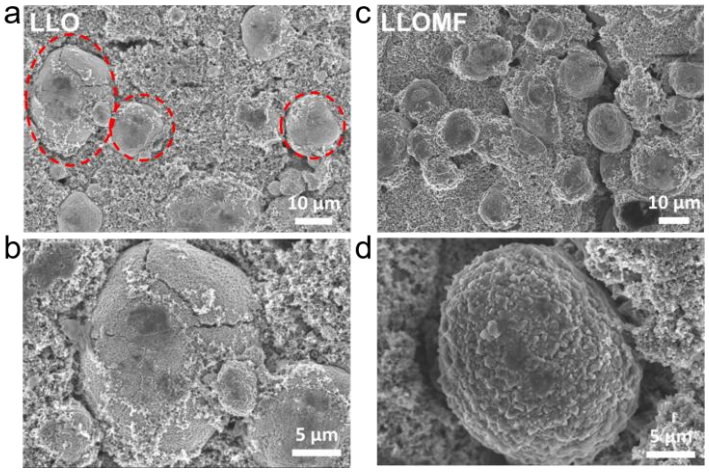

Fig. S50 Surface morphology of LLO and LLOMF after 200 cycles. (a, b) SEM images of LLO (a) after 200 cycles at 1 C and the enlarged images (b). (c, d) SEM images of LLOM (c) after 200 cycles at 1 C and the enlarged images (d).

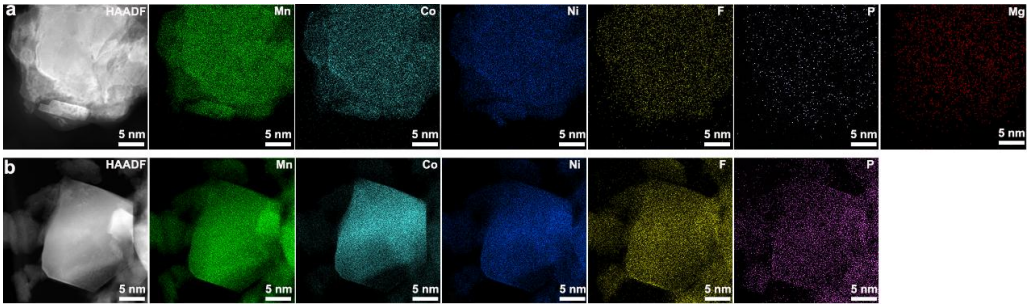

Fig. S51 HAADF-STEM and EDS mapping images show the distribution of Mn, Co, Ni, Mg, P, and F elements in the electrodes of LLOMF (a) and LLO (b) samples after 200 cycles.

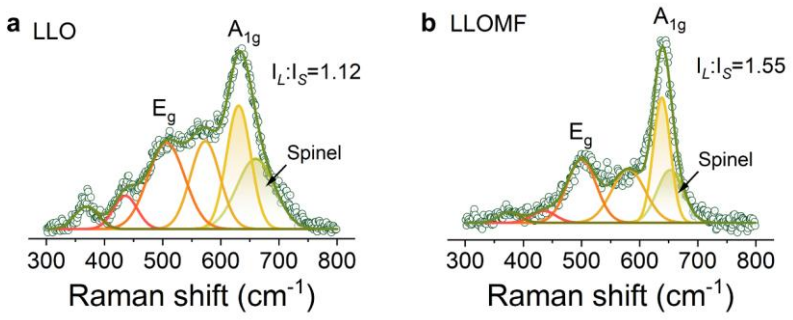

Fig. S52 Raman spectra and fitting results of LLO (a) and LLOMF (b) after 200 cycles.

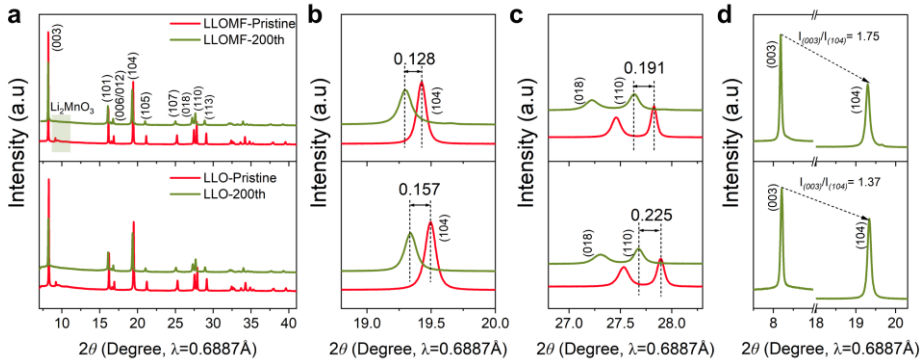

Fig. S53 (a) SXRD patterns of the cycled LLOMF (top) and LLO (bottom) after 200 cycles at 1.0 C. (b~d) Detail of the (104) (b), (018)/(110) (c) and (003)/(104) (d) diffraction peak for fresh and cycled samples.

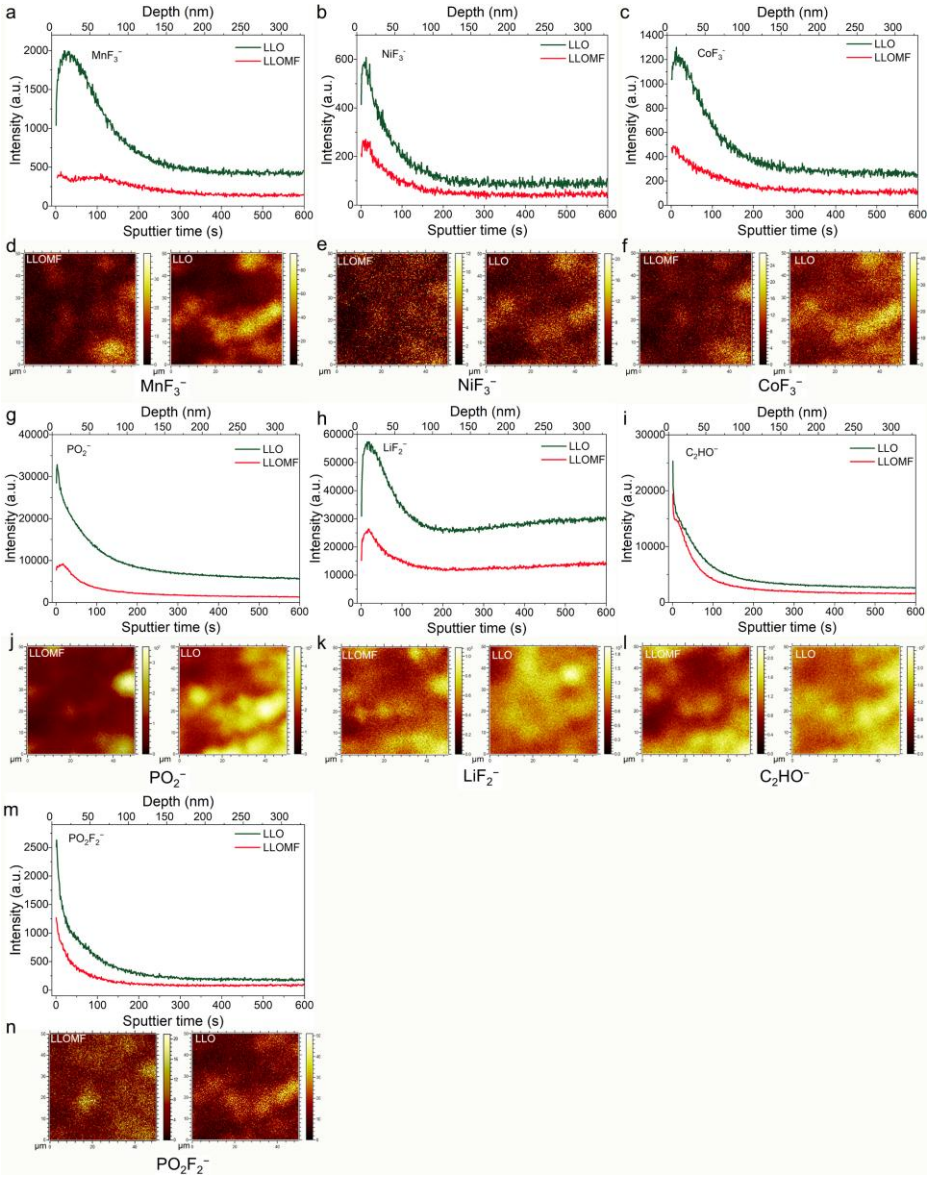

Fig. S54 TOF-SIMS depth profile shows the distribution of MnF_3^- (a), NiF_3^- (b), CoF_3^- (c), PO_2^- (g), LiF_2^- (h), C_2HO^- (i), and $PO_2F_2^-$ (m) fragments in the electrode after 200 cycles for LLO and LLOMF. g) The TOF-SIMS two-dimensional depth image shows the distribution of MnF_3^- (d), NiF_3^- (e), CoF_3^- (f), PO_2^- (j), LiF_2^- (k), C_2HO^- (l), and $PO_2F_2^-$ (n) fragments under LLO (left) and LLOMF (right) cycling conditions.

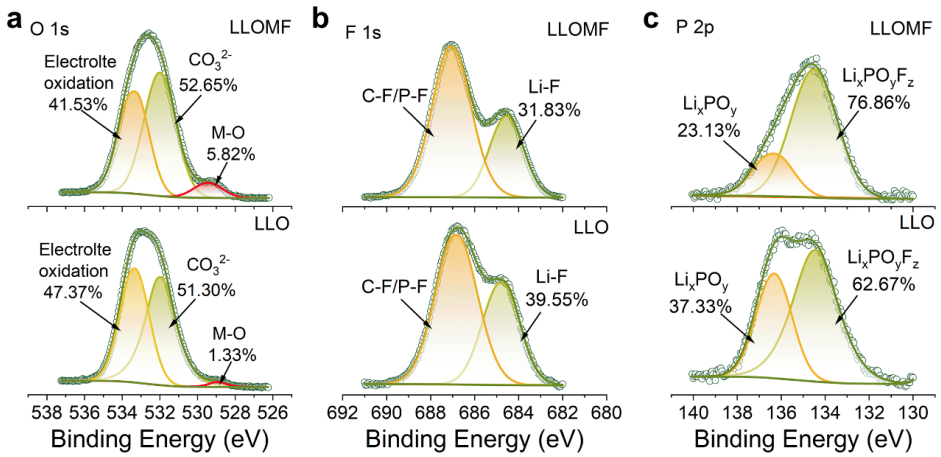

Fig. S55 (a~c) Comparison of O 1s (a), F 1s (b), and P 2p (c) by XPS on the cycled LLOMF (top) and LLO (bottom).

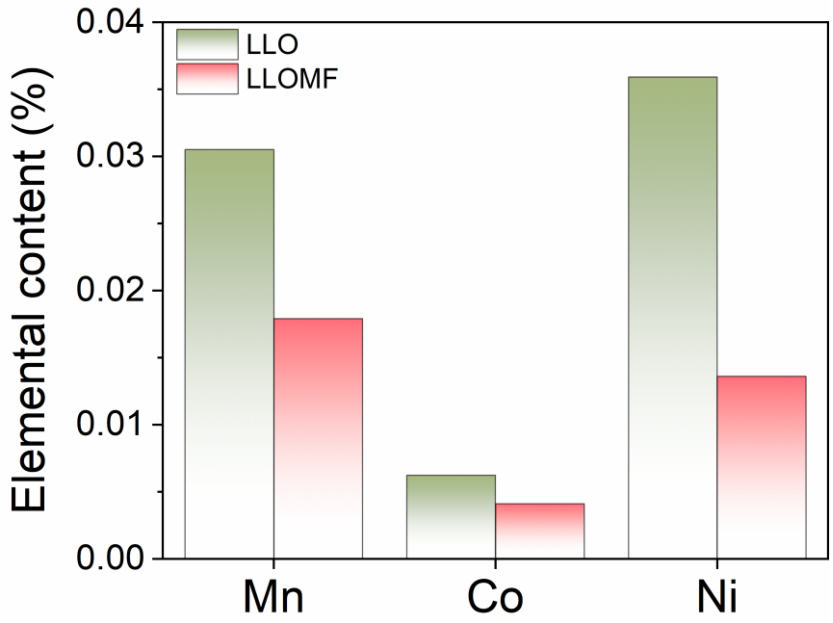

Fig. S56 ICP-OES quantitative analysis of dissolved Mn, Co, and Ni contents in the electrolytes of LLO and LLOMF electrodes after 200 cycles at 1 C (2.0–4.6 V)

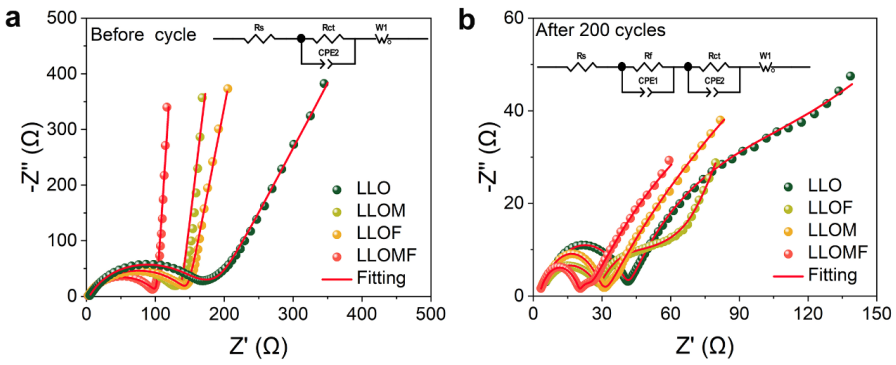

Fig. S57 EIS Nyquist plots and their fitting results for LLO and LLOMF before cycle (a) and after 200 cycles (b).

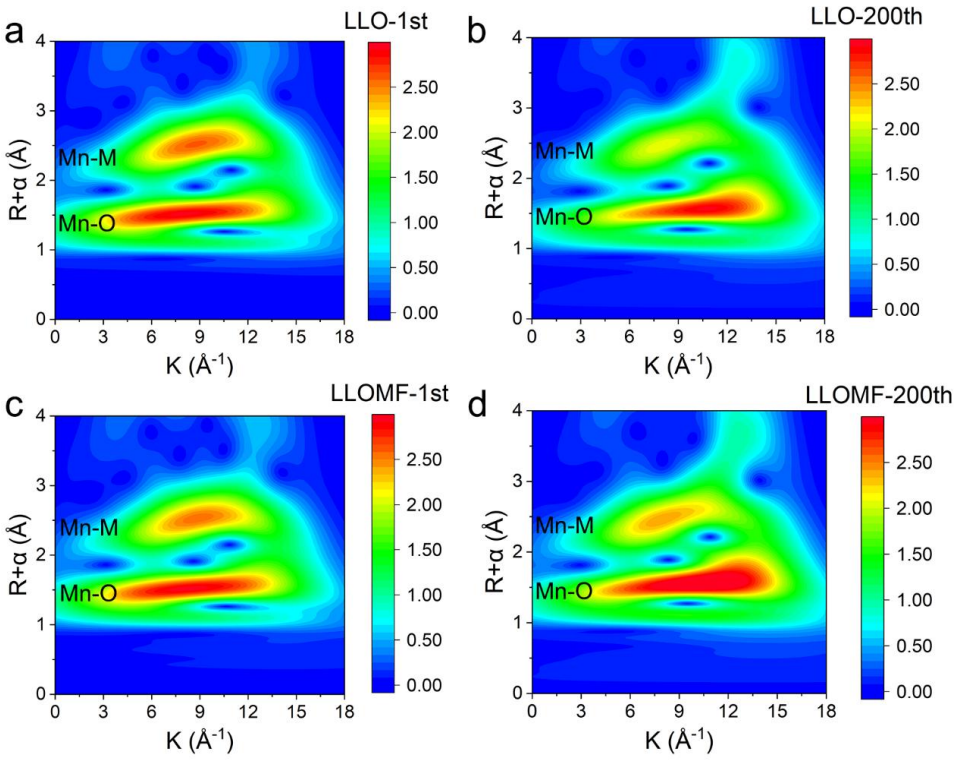

Fig. S58 (a, b) Wavelet transform of Mn K-edge EXAFS spectra after the 1st (a) and 200th (b) cycles of LLO. (c, d) Wavelet transform of Mn K-edge EXAFS spectra after the 1st (c) and 200th (d) cycles of LLOMF.

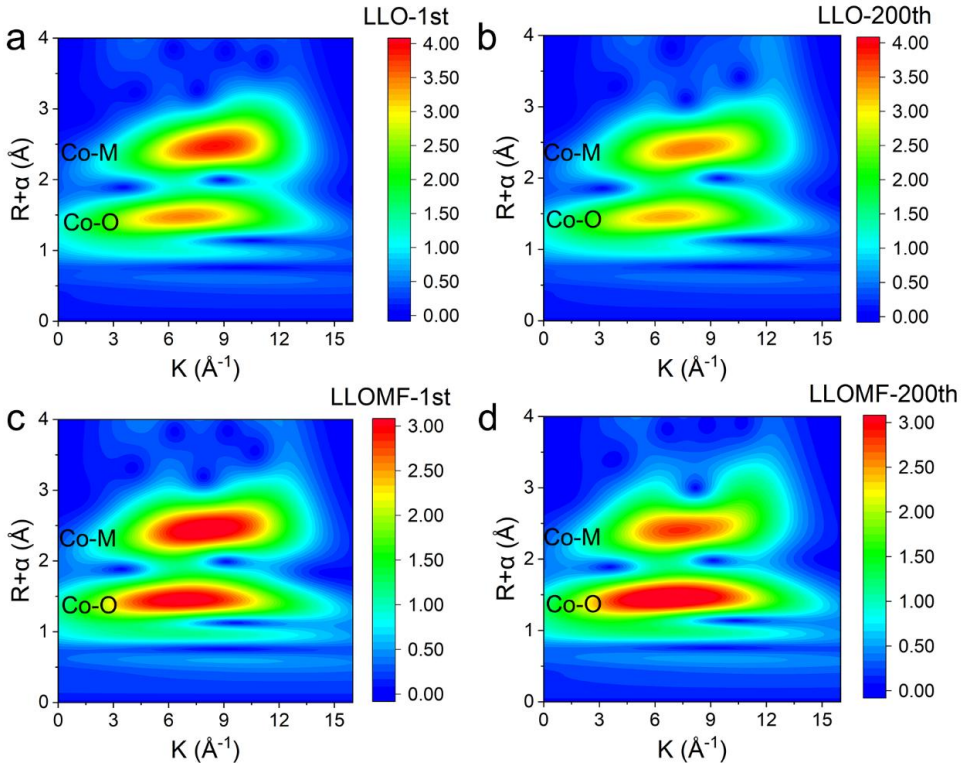

Fig. S59 (a, b) Wavelet transform of Co K-edge EXAFS spectra after the 1st (a) and 200th (b) cycles of LLO. (c, d) Wavelet transform of Co K-edge EXAFS spectra after the 1st (c) and 200th (d) cycles of LLOMF.

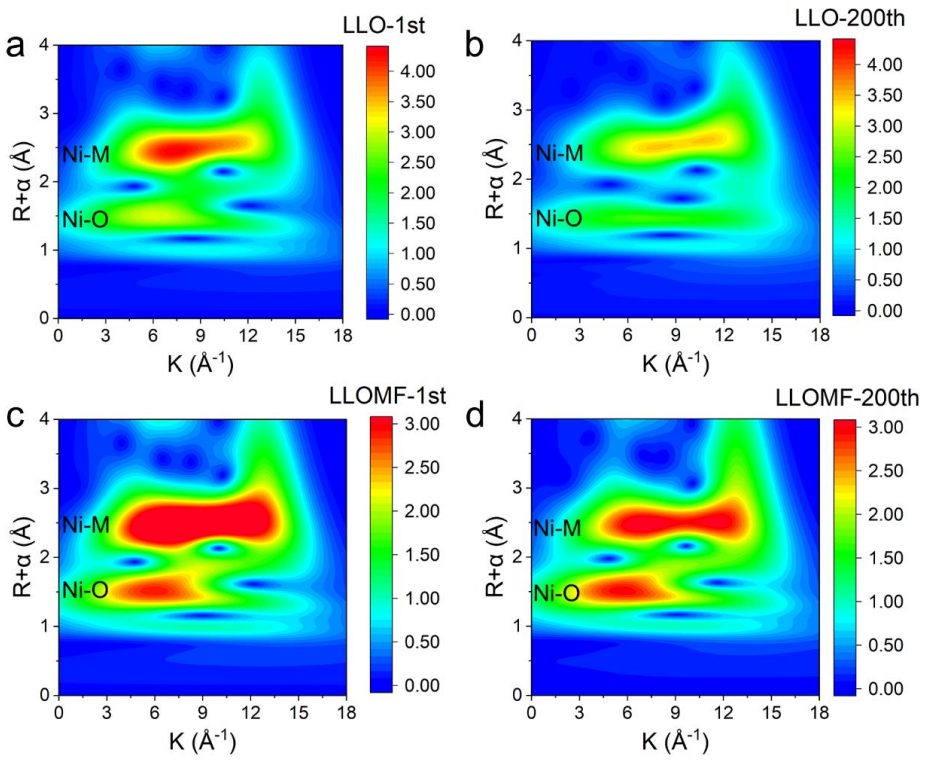

Fig. S60 (a, b) Wavelet transform of Ni K-edge EXAFS spectra after the 1st (a) and 200th (b) cycles of LLO. (c, d) Wavelet transform of Ni K-edge EXAFS spectra after the 1st (c) and 200th (d) cycles of LLOMF.

Supplementary Tables

Table S1 ICP-OES (Li, Ni, Co, Mn, Mg) and F-ISE (F) quantified compositions analysis results for pristine LLO, LLOM, LLOF, and LLOMF samples.

Sample	Li	Ni	Co	Mn	Mg	F
LLO	1.1543	0.1405	0.1307	0.5432	0	0
LLOF	1.0815	0.1406	0.1334	0.5505	0	0.0353
LLOM	1.1475	0.1401	0.1309	0.5425	0.0046	0
LLOMF	1.1302	0.1400	0.1305	0.5389	0.0045	0.0339

Table S2 Joint Rietveld refinement results of X-ray diffraction (SXRD) and neutron powder diffraction(NPD).

Sample	a(Å)	c(Å)	V(Å^3)	Microstrin (%)	Fd-3m phase ratio (%)	Li/Ni mixing (%)	Ov. Content (%)
LLO	2.85184 (39)	14.24712 (12)	100.348 (13)	0.152 (2)	0.506 (3)	2.02 (8)	1.02 (4)
LLOM	2.85255 (5)	14.24733 (21)	100.399 (30)	0.147 (4)	0.372 (2)	1.63 (14)	0.92 (5)
LLOF	2.85324 (7)	14.24918 (30)	100.461 (3)	0.421 (2)	7.006 (4)	1.79 (18)	4.09 (8)
LLOMF	2.85447 (6)	14.24864 (25)	100.519 (4)	0.501 (3)	6.239 (3)	1.27 (9)	5.67 (6)

Table S3 Joint Rietveld refinement of X-ray diffraction (SXRD) and neutron powder diffraction(NPD) data for LLO material.

Space group: R-3m and Fd-3m R_{wp}= 7.39%

S(MO_2)=2.6628 Å *I*(LiO_2)=2.1209 Å

Atom	Wyckoff position	Coordinates			Occupancy
		x	y	z	
Li1	3a	0.0	0.0	0.0	0.9798(8)
Ni1	3a	0.0	0.0	0.0	0.0202(8)
Li2	3b	0.0	0.0	0.5	0.2202(8)
Ni2	3b	0.0	0.0	0.5	0.1098(8)
Co	3b	0.0	0.0	0.5	0.1300
Mn	3b	0.0	0.0	0.5	0.5400
O	6c	0.0	0.0	0.24110(3)	0.9898(4)

Table S4 Joint Rietveld refinement of X-ray diffraction (SXRD) and neutron powder diffraction(NPD) data for LLOM material.

Space group: R-3m and Fd-3m R_{wp}= 8.26%

S(MO_2)=2.5908 Å *I*(LiO_2)=2.1583 Å

Atom	Wyckoff position	Coordinates			Occupancy
		x	y	z	
Li1	3a	0.0	0.0	0.0	0.9837(14)
Ni1	3a	0.0	0.0	0.0	0.0163(14)
Li2	3b	0.0	0.0	0.5	0.2163(14)
Ni2	3b	0.0	0.0	0.5	0.1137(14)
Co	3b	0.0	0.0	0.5	0.1300
Mn	3b	0.0	0.0	0.5	0.5400
O	6c	0.0	0.0	0.24141(8)	0.9908(5)

Table S5 Joint Rietveld refinement of X-ray diffraction (SXRD) and neutron powder diffraction(NPD) data for LLOF material.

Space group: R-3m and Fd-3m R_{wp}= 8.65%

S(MO_2)=2.6333 Å *I*(LiO_2)=2.1164 Å

Atom	Wyckoff position	Coordinates			Occupancy
		x	y	z	
Li1	3a	0.0	0.0	0.0	0.9821(18)
Ni1	3a	0.0	0.0	0.0	0.0179(18)
Li2	3b	0.0	0.0	0.5	0.2179(18)
Ni2	3b	0.0	0.0	0.5	0.1121(18)
Co	3b	0.0	0.0	0.5	0.1300
Mn	3b	0.0	0.0	0.5	0.5400
O	6c	0.0	0.0	0.24093(7)	0.9591(8)

Table S6 Joint Rietveld refinement of X-ray diffraction (SXRD) and neutron powder diffraction(NPD) data for LLOMF material.

Space group: R-3m and Fd-3m R_{wp}= 6.99%

S(MO_2)=2.6187 Å *I*(LiO_2)=2.1308 Å

Atom	Wyckoff position	Coordinates			Occupancy
		x	y	z	
Li1	3a	0.0	0.0	0.0	0.9873(9)
Ni1	3a	0.0	0.0	0.0	0.02127(9)
Li2	3b	0.0	0.0	0.5	0.2127(9)
Ni2	3b	0.0	0.0	0.5	0.1173(9)
Co	3b	0.0	0.0	0.5	0.1300
Mn	3b	0.0	0.0	0.5	0.5400
O	6c	0.0	0.0	0.24144(5)	0.9433(6)

Table S7 Fitted EXAFS distortion factors (σ^2) and distances (R) for Mn-O coordination shells. σ^2 and R represent the average interatomic distance (half-path length), and the mean square relative displacement in R (disorder).

	Mn-O shell		
Samples	R (Å)	σ^2 (Å^2)	R-factor
LLO	1.89765 (151)	0.00112 (50)	0.017
LLOM	1.89657 (158)	0.00133 (52)	0.016
LLOF	1.89657 (157)	0.00159 (53)	0.017
LLOMF	1.89597 (170)	0.00167 (57)	0.019

Table S8 Fitted EXAFS distortion factors (σ^2) and distances (R) for Co-O coordination shells. σ^2 and R represent the average interatomic distance (half-path length), and the mean square relative displacement in R (disorder).

	Co-O shell		
Samples	R (Å)	σ^2 (Å^2)	R-factor
LLO	1.92184 (74)	0.00151 (25)	0.002
LLOM	1.91784 (71)	0.00195 (24)	0.003
LLOF	1.91760 (117)	0.00226 (40)	0.006
LLOMF	1.92465 (131)	0.00257 (26)	0.009

Table S9 Fitted EXAFS distortion factors (σ^2) and distances (R) for Ni-O coordination shells. σ^2 and R represent the average interatomic distance (half-path length), and the mean square relative displacement in R (disorder).

	Ni-O shell		
Samples	R (Å)	σ^2 (Å^2)	R-factor
LLO	2.02977 (194)	0.00347 (66)	0.021
LLOM	2.03493 (219)	0.00347 (76)	0.020
LLOF	2.03170 (208)	0.00382 (72)	0.024
LLOMF	2.04048 (186)	0.00395 (55)	0.008

Table S10 Electrochemical performances of rechargeable intercalation-type Li-rich cathode coin cells and other works reported recently.

Material	Method	ICE/0.1 C [%]	Voltage range	Mass capacity (mg cm^{-2})	Capacity retention (%)	Voltage decay (mV $cycle^{-1}$/%)	Ref.
$Li_{1.17}Ni_{0.14}Co_{0.14}Mn_{0.55}O_2$	La^{2+} doping	83.0%	2-4.8 V	3 mg cm^{-2}	82.1% (1 C, 200)	3.8 (1 C, 200)	*Angew. Chem. Int. Ed.,* 2025, 64, e202424079
$Li_{1.2}Mn_{0.54}Ni_{0.13}Co_{0.13}O_2$	Sorbic acid-assisted	88.3%	2-4.8 V	2~3 mg·cm^{-2}	87.91% (1 C, 150th)	1.26 (1 C, 150th)	*Angew. Chem. Int. Ed.,* 2025, 64, e202501539
$Li_{1.2}Co_{0.13}Ni_{0.13}Mn_{0.54}O_2$	Electrolyte modification	100%	2-4.8 V	3 mg cm^{-2}	82.5% (1 C, 250th)	1.4 (1 C, 100th)	*Angew. Chem. Int. Ed.,* 2025, 64 e202502603
$Li_{1.177}Ni_{0.127}Co_{0.130}Mn_{0.533}O_2$	Layered-spinel epitaxial structure	87.1%	2-4.8 V	2.5 mg cm^{-2}	81.0% (1 C, 500th)	1.15 (1 C, 500th)	*Energy Environ. Sci.*, 2025, 18, 1241-1254
$Li_{1.2}Co_{0.13}Ni_{0.13}Mn_{0.54}O_2$	boronation engineering	85.2%	2-4.8 V	2.26 mg cm^{-2}	86.8% (1 C, 500th)	0.788 (1 C, 500th)	*Energy Environ. Sci.*, 2025, 18, 6168-6179
$Li_{1.145}Ni_{0.135}Co_{0.136}Mn_{0.542}O_2$	Brine quenching	88%	2-4.8 V	6 mg·cm^{-2}	92.3% (1 C, 200th)	1.21 (1 C, 200th)	*Energy Environ. Sci.*, 2025, 18, 284-299
$Li_{1.2}Co_{0.13}Ni_{0.13}Mn_{0.54}O_2$	Urea phosphate modification	88.2%	2-4.7 V	2~3 mg·cm^{-2}	82.9% (1 C, 500th)	0.91 (1 C, 500th)	*Mater. Today*, https://doi.org/10.1016/j.mattod.2025.04.018
$Li_{1.2}Ni_{0.2}Mn_{0.6}O_2$	Electrolyte modification	/	2-4.8 V	/	71% (1 C, 800th)	0.847 (1 C, 800th)	*J. Am. Chem. Soc.,* 2024, 146, 4557−4569
$Li_{1.2}Co_{0.1}Ni_{0.1}Mn_{0.6}O_2$	Li/O dual vacancies	94%	2-4.6 V	/	91% (1 C, 200th)	1.97 (1 C, 200th)	*Adv. Funct. Mater.,* 2024, 34, 2401249
$Li_{1.2}Ni_{0.2}Mn_{0.6}O_2$	Electrolyte modification	90.1%	0.5-3.2 V	6 mg·cm^{-2}	91% (0.2 C, 100th)	1.88 (0.2 C, 100th)	*Adv. Energy Mater*., 2024, 14, 2401097.
$Li_{1.16}Ni_{0.28}Mn$	Lithium	/	2-4.7 V	10 mg·cm^{-2}	86.2%	4.46	*Energy Environ. Sci.,*

$_{0.56}O_2$	source regulation				(0.33 C, 100th)	(0.33 C, 50th)	2024,17, 4634-4645
$Li_{1.20}Ni_{0.32}Mn_{0.48}O_2$	Superstructure units design	78.4%	2-4.7 V	/	84.8% (1 C, 200th)	1.36 (1 C, 200th)	*Nat. Commun.,* 2024, 15, 9981
$Li_{1.2}Ni_{0.2}Mn_{0.6}O_2$	Anionic entropy design	97%	2-4.7 V	3 mg cm^{-2}	83% (1 C, 400th)	1.36 (1 C, 400th)	*Adv. Mater*., 2024, 36, 2413785
$Li_{1.2}Ni_{0.2}Mn_{0.6}O_2$	Li/Ni disordered design	87%	2-4.8 V	2~3 mg·cm^{-2}	86% (0.33 C, 500th)	1.45 (0.33 C, 300th)	*Adv. Mater.,* 2024, 36, 2404982.
$Li_{1.2}Co_{0.13}Ni_{0.13}Mn_{0.54}O_2$	Lattice Engineering	/	2-4.6 V	1.4~2 mg·cm^{-2}	80% (1 C, 400th)	0.74 (1 C, 400th)	*Adv. Mater.,* 2024, 2414786.
$Li_{1.2}Co_{0.13}Ni_{0.13}Mn_{0.54}O_2$	Nb_2O_5 treatment	85%	2-4.8 V	2.5 mg·cm^{-2}	81% (1 C, 300th)	/	*Angew. Chem. Int. Ed.,* 2025, 64, e202413563
$Li_{1.2}Co_{0.13}Ni_{0.13}Mn_{0.54}O_2$	Gas–solid Phosphating	88.3%	2-4.8 V	2 mg·cm^{-2}	82.1% % (1 C, 300th)	82.1% (1 C, 300th)	*Adv. Mater.,* 2025, 37, 2416136
$Li_{1.2}Co_{0.13}Ni_{0.13}Mn_{0.54}O_2$	Glyoxal treatment	97.1%	2-4.8 V	/	76.5% (0.5C, 250th)	87.2% (0.5 C, 250th)	*Angew. Chem. Int. Ed.,* 2025, 64, e202501777.
$Li_{1.2}Co_{0.13}Ni_{0.13}Mn_{0.54}O_2$	Oxygen framework design	97.4%	2-4.6 V	5.27 mg·cm^{-2}	81.3% (1 C, 800th)	0.64 (1 C, 800th)	This work

Table S11 Detailed information of pouch-type graphite||LLOMF full cell.

Electrode	Cathode LLOM	Anode Graphite
Surface load mass [mg cm^{-2}]	10	7.8
Active substance content [%]	92.0	93.5
Compaction density [g cm^{-3}]	2.3	1.6
Specific capacity [mAh g^{-1}]	265	350
Electrode size [mm^2]	62*72	64*74
N/P ratio	1.08	
Cell capacity [Ah]	1.5	

Table S12 Fitted EXAFS distortion factors (σ^2) and distances (R) for Mn-O coordination shells. σ^2 and R represent the average interatomic distance (half-path length), and the mean square relative displacement in R (disorder).

	Mn-O					
	LLO			LLOMF		
E (V)	R (Å)	σ^2 (Å^2)	R-factor	R (Å)	σ^2 (Å^2)	R-factor
Ch. 3.9 V	1.9089(10)	0.00162(91)	0.019	1.9072(11)	0.00243(57)	0.015
Ch. 4.4 V	1.9019(12)	0.00293(77)	0.012	1.8982(6)	0.00245(68)	0.011
Ch. 4.5 V	1.8970(11)	0.00341(71)	0.011	1.8944(11)	0.00235(65)	0.008
Ch. 4.8 V	1.8971(9)	0.00399(61)	0.007	1.8981(12)	0.00314(67)	0.006
Dis. 3.6 V	1.8995(9)	0.00391(60)	0.007	1.8986(13)	0.00332(72)	0.007
Dis. 2.8 V	1.9029(9)	0.00382(61)	0.006	1.9041(13)	0.00347(75)	0.007
Dis. 2.0 V	1.9032(10)	0.00419(57)	0.007	1.9067(4)	0.00355(62)	0.009

Table S13 Fitted EXAFS distortion factors (σ^2) and distances (R) for Co-O coordination shells. σ^2 and R represent the average interatomic distance (half-path length), and the mean square relative displacement in R (disorder).

	Co-O					
	LLO			LLOMF		
E (V)	R (Å)	σ^2 (Å^2)	R-factor	R (Å)	σ^2 (Å^2)	R-factor
Ch. 3.9 V	1.9182(7)	0.00218(53)	0.003	1.9181(12)	0.00266(84)	0.007
Ch. 4.4 V	1.8944(8)	0.00274(53)	0.003	1.8983(12)	0.00311(82)	0.007
Ch. 4.5 V	1.8899(9)	0.00312(58)	0.003	1.8974(12)	0.00368(83)	0.007
Ch. 4.8 V	1.8916(9)	0.00352(59)	0.003	1.8942(11)	0.00364(73)	0.005
Dis. 3.6 V	1.8963(10)	0.00344(70)	0.005	1.9021(13)	0.00365(88)	0.008
Dis. 2.8 V	1.9172(8)	0.00346(56)	0.003	1.92037(9)	0.00344(65)	0.005
Dis. 2.0 V	1.9304(3)	0.00325(43)	0.003	1.92383(7)	0.00303(78)	0.007

Table S14 Fitted EXAFS distortion factors (σ^2) and distances (R) for Ni-O coordination shells. σ^2 and R represent the average interatomic distance (half-path length), and the mean square relative displacement in R (disorder).

	Ni-O					
	LLO			LLOMF		
E (V)	R (Å)	σ^2 (Å^2)	R-factor	R (Å)	σ^2 (Å^2)	R-factor
Ch. 3.9 V	2.0306(27)	0.00342(90)	0.013	2.0302(27)	0.00396(140)	0.015
Ch. 4.4 V	1.8996(15)	0.00411(97)	0.008	1.9079(16)	0.00462(83)	0.007
Ch. 4.5 V	1.9019(14)	0.00477(91)	0.007	1.9099(17)	0.00491(85)	0.007
Ch. 4.8 V	1.8977(15)	0.00520(100)	0.009	1.9218(21)	0.00586(107)	0.010
Dis. 3.6 V	1.9046(20)	0.00493(131)	0.014	1.9412(28)	0.00558(109)	0.017
Dis. 2.8 V	2.0427(25)	0.00387(115)	0.012	2.0257(25)	0.00356(105)	0.019
Dis. 2.0 V	2.0548(19)	0.00466(142)	0.012	2.0371(19)	0.00378(109)	0.017

Table S15 Fitted EXAFS distortion factors (σ^2) and distances (R) for Mn-M coordination shells. σ^2 and R represent the average interatomic distance (half-path length), and the mean square relative displacement in R (disorder).

	Mn-M					
	LLO			LLOMF		
E (V)	R (Å)	σ^2 (Å^2)	R-factor	R (Å)	σ^2 (Å^2)	R-factor
Ch. 3.9 V	2.8388(21)	0.00116(42)	0.019	2.8491(15)	0.00119(71)	0.015
Ch. 4.4 V	2.8180(16)	0.00267(82)	0.012	2.8169(15)	0.00256(84)	0.011
Ch. 4.5 V	2.8206(14)	0.00307(74)	0.011	2.8204(15)	0.00349(76)	0.008
Ch. 4.8 V	2.8346(10)	0.00521(55)	0.007	2.8368(15)	0.00462(59)	0.006
Dis. 3.6 V	2.8384(10)	0.00483(53)	0.007	2.8383(15)	0.00436(65)	0.007
Dis. 2.8 V	2.8579(10)	0.00336(53)	0.006	2.8529(15)	0.00347(63)	0.007
Dis. 2.0 V	2.8616(11)	0.00376(52)	0.007	2.8580(15)	0.00344(58)	0.009

Table S16 Fitted EXAFS distortion factors (σ^2) and distances (R) for Co-M coordination shells. σ^2 and R represent the average interatomic distance (half-path length), and the mean square relative displacement in R (disorder).

	Co-M					
	LLO			LLOMF		
E (V)	R (Å)	σ^2 (Å^2)	R-factor	R (Å)	σ^2 (Å^2)	R-factor
Ch. 3.9 V	2.8234(10)	0.00344(49)	0.003	2.825(16)	0.00524(85)	0.007
Ch. 4.4 V	2.8073(9)	0.00448(48)	0.003	2.8207(15)	0.00607(83)	0.007
Ch. 4.5 V	2.8067(10)	0.0050(51)	0.003	2.8153(15)	0.00625(78)	0.007
Ch. 4.8 V	2.8091(10)	0.00587(50)	0.003	2.8204(13)	0.00719(69)	0.005
Dis. 3.6 V	2.8097(12)	0.00565(62)	0.005	2.8226(15)	0.00629(83)	0.008
Dis. 2.8 V	2.8317(10)	0.00596(48)	0.003	2.8386(5)	0.00646(61)	0.005
Dis. 2.0 V	2.8379(3)	0.00548(38)	0.003	2.8392(8)	0.00615(84)	0.007

Table S17 Fitted EXAFS distortion factors (σ^2) and distances (R) for Ni-M coordination shells. σ^2 and R represent the average interatomic distance (half-path length), and the mean square relative displacement in R (disorder).

	Ni-M					
	LLO			LLOMF		
E (V)	R (Å)	σ^2 (Å^2)	R-factor	R (Å)	σ^2 (Å^2)	R-factor
Ch. 3.9 V	2.8806(22)	0.00776(117)	0.013	2.8883(22)	0.00968(61)	0.015
Ch. 4.4 V	2.8403(15)	0.00628(66)	0.008	2.8472(14)	0.00774(69)	0.007
Ch. 4.5 V	2.8314(14)	0.00608(67)	0.007	2.8414(15)	0.00744(71)	0.007
Ch. 4.8 V	2.8281(15)	0.00720(75)	0.009	2.8408(18)	0.00784(91)	0.010
Dis. 3.6 V	2.8350(18)	0.00816(90)	0.014	2.8485(24)	0.00823(119)	0.017
Dis. 2.8 V	2.8779(22)	0.00940(116)	0.012	2.8757(23)	0.00938(116)	0.019
Dis. 2.0 V	2.8959(8)	0.00992(109)	0.012	2.8894(7)	0.00984(100)	0.017

Notes and references

1. B. Qiu, M. Zhang, L. Wu, J. Wang, Y. Xia, D. Qian, H. Liu, S. Hy, Y. Chen, K. An, Y. Zhu, Z. Liu and Y. S. Meng, *Nature Communications*, 2016, **7**, 12108.
2. B. Ravel and M. Newville, *J. Synchrotron Radiat.*, 2005, **12**, 537-541.
3. B. H. Toby and R. B. Von Dreele, *J Appl Crystallogr*, 2013, **46**, 544-549.
4. H. Dau, P. Liebisch and M. Haumann, *Anal. Bioanal. Chem.*, 2003, **376**, 562-583.
5. L. Zeng, K. Shi, B. Qiu, H. Liang, J. Li, W. Zhao, S. Li, W. Zhang, Z. Liu and Q. Liu, *Chem. Eng. J.*, 2022, **437**, 135276.
6. G. Kresse and D. Joubert, *Physical Review B*, 1999, **59**, 1758-1775.
7. G. Kresse and J. Hafner, *Physical Review B*, 1993, **47**, 558-561.
8. J. P. Perdew, K. Burke and M. Ernzerhof, *Phys. Rev. Lett.*, 1996, **77**, 3865-3868.
9. F. Zhou, M. Cococcioni, C. A. Marianetti, D. Morgan and G. Ceder, *Physical Review B*, 2004, **70**, 235121.
10. H. J. Monkhorst and J. D. Pack, *Physical Review B*, 1976, **13**, 5188-5192.
11. H. Zheng, Z. Hu, P. Liu, W. Xu, Q. Xie, W. He, Q. Luo, L. Wang, D. Gu, B. Qu, Z.-Z. Zhu and D.-L. Peng, *Energy Storage Mater.*, 2020, **25**, 76-85.
12. B. Qiu, Q. Zhang, H. Hu, J. Wang, J. Liu, Y. Xia, Y. Zeng, X. Wang and Z. Liu, *Electrochim. Acta*, 2014, **123**, 317-324.